

# Testing QUMOND theory with Galactic globular clusters in a weak external field

A. Sollima<sup>1\*</sup>†, C. Nipoti<sup>2‡</sup>, F. Calura<sup>1</sup>, R. Pascale<sup>1</sup>, H. Baumgardt<sup>3</sup>

<sup>1</sup>*INAF Osservatorio di Astrofisica e Scienza dello spazio di Bologna, via Gobetti 93/3, 40129 Bologna, Italy*

<sup>2</sup>*Dipartimento di Fisica e Astronomia "Augusto Righi", Università di Bologna, via Gobetti 93/2, 40129 Bologna, Italy*

<sup>3</sup>*School of Mathematics and Physics, University of Queensland, St Lucia, QLD 4072, Australia*

Accepted 2023 July 18. Received 2023 July 14; in original form 2023 May 16

## ABSTRACT

We developed self-consistent dynamical models of stellar systems in the framework of quasi-linear modified Newtonian dynamics (QUMOND). The models are constructed from the anisotropic distribution function of Gunn & Griffin (1979), combined with the modified Poisson equation defining this gravitation theory and take into account the external field effect. We have used these models, and their Newtonian analogues, to fit the projected density and the velocity dispersion profiles of a sample of 18 Galactic globular clusters, using the most updated datasets of radial velocities and Gaia proper motions. We have thus obtained, for each cluster, estimates of the dynamical mass-to-light ratio ( $M/L$ ) for each theory of gravity. The selected clusters have accurate proper motions and a well sampled mass function down to the very low mass regime. This allows us to constrain the degree of anisotropy and to provide, from comparison with stellar evolution isochrones, a dynamics-independent estimate of the minimum mass-to-light ratio  $(M/L)_{min}$ . Comparing the best-fitting dynamical  $M/L$  with  $(M/L)_{min}$ , we find that for none of the analyzed clusters the two gravity theories are significantly incompatible with the observational data, although for one of them (NGC 5024) the dynamical  $M/L$  predicted by QUMOND lies at  $2.8\sigma$  below  $(M/L)_{min}$ . Though the proposed approach suffers from some limitations (in particular the lack of a treatment of mass segregation), the obtained results suggest that the kinematics of globular clusters in a relatively weak external field can be a powerful tool to prove alternative theories of gravitation.

**Key words:** gravitation – methods: data analysis – stars: kinematics and dynamics – globular clusters: general

## 1 INTRODUCTION

One of the most astonishing astronomical discovery of the 20th century has been the tension between the estimate of the mass budget through luminous and dynamical tracers, suggesting the existence of a large amount of "dark matter". Such an evidence was first noticed by Zwicky (1933, 1937) as an anomaly in the velocity of galaxies inside the Coma cluster, and later confirmed at all scales, in the rotation of galactic disks (Babcock 1939; Kent 1986; Korsaga et al. 2019), in the mass-to-light ratio of dwarf spheroidal galaxies (Faber & Lin 1983; Walker et al. 2009), in the gravitational lensing of background objects by galaxy clusters (Wu et al. 1998; Clowe et al. 2006), in the temperature distribution of hot gas in galaxies and clusters (Mushotzky 1991; Mulchaey et

al. 1993), and in the pattern of anisotropies in the cosmic microwave background (Smoot et al. 1992; Planck Collaboration et al. 2016). According to the last estimate provided by the Planck satellite (Planck Collaboration et al. 2020)  $\sim 85\%$  of the mass budget of the Universe is constituted by non-baryonic matter. The freedom in the distribution of the dark mass in general allows one to solve the aforementioned tensions, so the dark matter paradigm is very hard to disprove. Nevertheless, despite the large effort in searching for dark matter particles, there has been no well-established detection of dark matter from a direct detection experiment (Carmona-Benitez et al. 2016; XENON Collaboration et al. 2020).

Since the early '80s, Milgrom (1983) hypothesized an alternative explanation, postulating a modification of the standard Newtonian gravitation law at the regime of very low accelerations ( $< 10^{-10}$  m/s<sup>2</sup>), known as modified Newtonian dynamics (MOND). In particular, in spherical symmetry, the MOND gravitational field  $-\nabla\phi_M$  is related to the Newtonian gravitational field  $-\nabla\phi_N$  by

$$\nabla\phi_M \mu(\|\nabla\phi_M\|/a_0) = \nabla\phi_N, \quad (1)$$

where  $a_0$  is a characteristic acceleration ( $a_0 \approx 1.2 \times$

\* Deceased.

† We dedicate this paper to the memory of our dear friend and colleague Antonio Sollima, who passed away prematurely a few months ago. Antonio was a generous and witty person, and a creative and brilliant scientist, whom we miss deeply. Antonio conceived, developed and carried out most of this work, which we have had the honour to finalize.

‡ E-mail: carlo.nipoti@unibo.it

$10^{-10} \text{ m/s}^2$ ) and  $\mu$  is a function that smoothly runs from  $\mu(x) \sim x$  when  $x \ll 1$  to  $\mu(x) \sim 1$  when  $x \gg 1$ .

So, any stellar system behaves as Newtonian when  $\|\nabla\phi_N\| \gg a_0$ , while its gravitational field deviates from Newtonian prediction as  $\|\nabla\phi_M\| \sim \sqrt{a_0\|\nabla\phi_N\|} > \|\nabla\phi_N\|$  when  $\|\nabla\phi_N\| \ll a_0$ . As a consequence, objects crossing regions characterized by low acceleration move faster in MOND than in Newtonian gravity, which potentially can solve the tension between luminous and dynamical mass without the need of dark matter. Such a simple and elegant modification, beside solving the dark matter issue, naturally reproduces the scaling relations of rotation- and pressure-supported galaxies like the Tully-Fisher (Tully & Fisher 1977) and Faber-Jackson (Faber & Jackson 1976) relations.

Following Milgrom's original idea, a few non-relativistic (see Bekenstein & Milgrom 1984; Milgrom 2010, 2023) and relativistic (see Bekenstein 2004; Famaey & McGaugh 2012; Skordis & Złoźnik 2021) MOND Lagrangian theories have been developed, such that the non-relativistic MOND gravitational field behaves essentially as in eq. (1). In this work, we consider in particular the non-relativistic formulation of Milgrom (2010), dubbed quasi-linear MOND (QUMOND), where the potential can be derived from the canonical Poisson equation adopting a "fake" density derivable from the actual density and the corresponding Newtonian potential. This theory thus involves solving only linear differential equations, with one non-linear, algebraic step. The QUMOND potential  $\phi_M$  obeys the equation

$$\nabla^2 \phi_M = \nabla \cdot [\nu(y)\nabla\phi_N] \quad (2)$$

or

$$\nabla^2 \phi_M = 4\pi G \rho_f, \quad (3)$$

where  $y = \|\nabla\phi_N\|/a_0$ , and  $\rho_f \equiv \nabla \cdot [\nu(y)\nabla\phi_N]/(4\pi G)$  is the fake density which is the source term of the canonical Poisson equation for  $\phi_M$ . The function  $\nu$  is linked to the interpolating function so that  $\mu(x)\nu(x\mu(x)) = 1$ .

Over the years, MOND has been remarkably successful, resisting several attempts of falsification (see Sanders & McGaugh 2002; Bekenstein 2009). However, some features of observed systems and astrophysical phenomena are problematic for MOND, such as the dynamics and lensing of clusters of galaxies (The & White 1988; Clowe et al. 2006; Nataraian & Zhao 2008), the survival of the Fornax dwarf galaxy globular cluster system (Nipoti et al. 2008), the internal and systemic dynamics of ultra faint dwarf galaxies (Safarzadeh & Loeb 2021), the rotation curve of bulge dominated galaxies (Fraternali, Sancisi, & Kamphuis 2011), the X-ray isophotes of bright elliptical galaxies (Buote & Canizares 1994; Angus, Famaey, & Buote 2008), the vertical kinematics of the Milky Way (Nipoti et al. 2007; Lisanti et al. 2019), the resolved kinematics of the ultra-diffuse galaxy AGC114905 (Mancera Piña et al. 2022) and the phenomenon of galaxy merging (Nipoti, Londrillo, & Ciotti 2007).

Another powerful class of objects useful to test this modified theory of gravitation is constituted by globular clusters (GCs; Baumgardt, Grebel, & Kroupa 2005). They are almost spherical systems whose kinematics is determined by the balance between the gravitational force and the pressure due to the internal motions of their stars. Although the majority of GCs have dense cores and therefore internal accelerations exceeding  $a_0$  by orders of magnitudes, the gravitational ac-

celeration quickly decreases with the distance often reaching values below  $a_0$  in their outskirts. So, the kinematics of an isolated GC with a sufficiently large radius is expected to be significantly different in Newtonian and MOND theories.

GCs are immersed in the Milky Way gravitational field whose strength is larger than  $a_0$  at Galactocentric distances  $R_{GC} < 12$  kpc (including  $\sim 71\%$  of the Galactic GC system). Note that, for a satellite stellar system such as a GC, the gravitational field that appears in the argument of  $\mu$  in eq. 1 is due to the contributions of both the satellite and the host system. So, in MOND, even a uniform external field affects the internal kinematics of a stellar system (the so-called "external field effect"; Bekenstein & Milgrom 1984). However, the few GCs populating the outer halo of the Milky Way feel negligible external accelerations ( $\|\mathbf{a}_{\text{ext}}\| \ll a_0$ ) and are extended enough to show significant differences in their velocity dispersion profiles according to the Newtonian dynamics and MOND (Baumgardt, Grebel, & Kroupa 2005; Sollima & Nipoti 2010; Ibata et al. 2011a,b), and therefore constitute an ideal tool to test these theories.

Two GCs have been analysed with this purpose till now: Palomar 14 and NGC 2419. Jordi et al. (2009) compared the projected velocity dispersion of Palomar 14 calculated with radial velocities of 17 member stars with a set of  $N$ -body simulations, reporting that the expected velocity dispersion in MOND is more than three times higher than the observed value, and concluded that this evidence challenges MOND. On the other hand, Gentile et al. (2010) claimed that the confidence level achievable using the small sample of stars used by Jordi et al. (2009) does not allow one to draw any significant conclusion on the validity of MOND. Finally, Sollima et al. (2012) performed  $N$ -body simulations of Palomar 14 in both Newtonian gravity and MOND investigating the effect of different assumptions on the mass-to-light ratio  $M/L$ , binary fraction, anisotropy in the stellar velocity distribution, and cluster orbit. Comparing mock observations constructed from these simulations and the spectroscopic sample of Jordi et al. (2009), they concluded that both Newtonian and MOND models acceptably reproduce observations, with MOND models preferring low  $M/L$ . They also found that even the weak external acceleration ( $\|\mathbf{a}_{\text{ext}}\| \simeq 0.16a_0$ ) felt by this GC produces significant effects on its kinematics.

Deeper analyses have been conducted on NGC2419. This GC is located at  $\approx 96$  kpc from the Galactic centre, thus feeling a negligible external field ( $\|\mathbf{a}_{\text{ext}}\| < 0.1a_0$ ). Moreover, it is massive enough ( $M \simeq 9.71 \times 10^3 M_\odot$ ; Baumgardt & Hilker 2018) to contain hundreds of bright stars with accurate radial velocities. Ibata et al. (2011a,b) used a large sample of  $\sim 160$  radial velocities and compared their velocity distribution with a set of dynamical models including the effect of anisotropy and binary fraction. They found that Newtonian models fit observations better than MOND providing likelihood larger by factor  $10^5$ . These results on NGC2419 have been however criticized by Sanders (2012a,b) who argued that polytropic MOND models provide a reasonable fit to the data and claimed that likelihood-based analyses *a)* are dependent on the choice of the model stellar phase-space distribution function and *b)* can be used in a comparative test between different classes of models, but cannot rule out a model which adequately reproduces observations.

A sound test to modified gravity would require the use of *i)* a simple and robust observational quantity which is as

much as possible independent on the underlying distribution function, and *ii*) models flexible enough to reproduce those dynamical properties of the system (e.g. anisotropy) whose degrees of freedom are all well constrained.

The shape and amplitude of the velocity dispersion profile (the main kinematic quantity used as observational constraint) in any dynamical model depend on the adopted  $M/L$  and on the degree of anisotropy. So, for a given pair of density and velocity dispersion profile, and once the anisotropy profile is fixed from the distribution of transverse motions, different gravitation theories will predict different dynamical  $M/L$ .

The cluster  $M/L$  is therefore an excellent tool to test gravitation theories. Indeed, as discussed above, for a given mass, MOND models predict velocity dispersions systematically higher than Newtonian ones. This is a property set by construction (linked to the increased acceleration of MOND below  $a_0$ ) and it is independent of the adopted distribution function. So, for a given velocity dispersion, MOND models require lower masses (and therefore  $M/L$ ) than Newtonian ones.

The  $M/L$  of a GC can be derived also with a method that is completely independent of dynamics, i.e. by summing the masses of individual stars detectable in deep photometric studies. This last task requires, beside a deep and complete photometry, the knowledge of the cluster mass function (MF) down to the faintest (lowest mass) stars and a stellar isochrone with suitable age and metallicity. Comparing the dynamical  $M/L$  with such dynamics-independent  $M/L$  is thus a powerful method to test gravitational theories on the scale of GCs.

Unfortunately, even the deepest photometric studies performed with the Hubble Space Telescope on a large number of GCs (Sarajedini et al. 2007) are limited to the inner halo (at  $R_{GC} < 30$  kpc). Similarly, the exquisite accuracy of proper motions provided by Gaia ( $\sigma_\mu = 25 \mu\text{as}/\text{yr}$  at  $V \sim 16$ ; Gaia Collaboration et al. 2018a) translate into several km/s beyond  $R_{GC} \sim 25$  kpc. For GCs in this distance range the acceleration exerted by the Milky Way gravitational field can be several times  $a_0$  and the external field effect cannot be neglected.

Dealing with the external field effect is technically simpler in QUMOND than, for instance, in the Bekenstein & Milgrom (1984) formulation of MOND (see, e.g., Lüghausen, Famaey, & Kroupa 2015 and Chae & Milgrom 2022), which makes QUMOND the natural choice if one wants to test MOND also with the GCs of the inner halo. These GCs are close enough to have well sampled MF down to the hydrogen burning limit (Paust et al. 2010; Sollima & Baumgardt 2017b; Ebrahimi et al. 2020; Baumgardt et al. 2023) and proper motions with accuracies comparable with those of radial velocities for hundreds of stars (Gaia Collaboration et al. 2021).

In this paper we present self-consistent dynamical models in the QUMOND theory that are analogues of those of Gunn & Griffin (1979) in Newtonian gravity. We then use these models to derive the dynamical mass-to-light ratio in the V band ( $M/L_V$ ) by best fitting the line-of-sight and transverse velocity distributions provided by the most updated compilation of radial velocities (Baumgardt & Hilker 2018) and Gaia proper motions for a sample of 18 Galactic GCs located between 2.5 and 18.5 kpc from the Galactic centre, in a regime of relatively weak ( $0.3 < a_{ext}/a_0 < 4.9$ ) external acceleration.

The comparison with the  $M/L_V$  derived independently using the observed MF, age, metallicity and theoretical isochrones is used to test both Newtonian and QUMOND theories.

In Sect. 2 the models are presented. In Sect. 3 we describe the selected sample of GCs and the dataset used in this analysis. Sect. 4 is devoted to the description of the algorithm used to derive the  $M/L_V$  from dynamics and its lower limit set from stellar models, together with their corresponding uncertainties. The results are presented in Sect. 5 and discussed in Sect. 6.

## 2 MODELS

### 2.1 Model description

For both Newtonian and QUMOND models we adopted the distribution function defined by Gunn & Griffin (1979, based on Michie 1963 and King 1966)

$$f(E, L) = \exp\left(-\frac{L^2}{2\sigma_K^2 r_a^2}\right) \left[ \exp\left(-\frac{E}{\sigma_K^2}\right) - 1 \right], \quad (4)$$

which can be written as

$$f(r, v_r, v_t) = \exp\left(-\frac{v_t^2 r^2}{2\sigma_K^2 r_a^2}\right) \left[ \exp\left(-\frac{v_r^2 + v_t^2}{2\sigma_K^2} - \frac{\phi(r)}{\sigma_K^2}\right) - 1 \right], \quad (5)$$

where  $E$  and  $L$  are the energy and angular momentum per unit mass,  $r$  is the distance from the cluster centre,  $\phi$  is the gravitational potential,  $r_a$  is the characteristic radius beyond which orbits become significantly radially biased,  $\sigma_K^2$  is an energy normalization, and  $v_r$  and  $v_t$  are the radial and tangential components of the velocity, respectively. The above distribution function represents the phase-space density and can be integrated over the velocity domain to obtain, as functions of radius, the density

$$\rho = 4\pi \int_0^{\sqrt{-2\phi}} dv_r \int_0^{\sqrt{-2\phi - v_r^2}} dv_t v_t f(r, v_r, v_t), \quad (6)$$

and the radial ( $\sigma_r$ ) and tangential ( $\sigma_t$ ) velocity dispersions, which are given by

$$\sigma_r^2 = \frac{4\pi}{\rho} \int_0^{\sqrt{-2\phi}} dv_r v_r^2 \int_0^{\sqrt{-2\phi - v_r^2}} dv_t v_t f(r, v_r, v_t), \quad (7)$$

and

$$\sigma_t^2 = \frac{4\pi}{\rho} \int_0^{\sqrt{-2\phi}} dv_r \int_0^{\sqrt{-2\phi - v_r^2}} dv_t v_t^3 f(r, v_r, v_t), \quad (8)$$

respectively. The differential equation linking the potential derivatives to the density is the canonical Poisson equation

$$\nabla^2 \phi_N = 4\pi G \rho \quad (9)$$

in the the Newtonian case, and eq. (3) in the QUMOND case. In all our MOND models we adopt the so-called "simple" interpolating function  $\mu(x) = x/(1+x)$  (Famaey & Binney 2005), whose corresponding  $\nu$  function is

$$\nu(y) = 1 + \frac{2}{y + \sqrt{y^2 + 4y}}. \quad (10)$$

In the Newtonian case eq. 9, coupled with eq. 6, can be solved in a straightforward way starting from a boundary

condition at the centre for the potential  $\phi = \phi_0$  and integrating eq. 6 outwards out to where the potential and the density vanish. In the QUMOND case the situation is more complex because eq. 6 provides, for a given potential  $\phi_M$ , the actual density  $\rho$ , while eq. 3 requires the fake density  $\rho_f$ . Note however that the relation between  $\rho$  and  $\rho_f$  can be derived by combining eq.s 2 and 3:

$$\rho_f = \nu\rho + \frac{\nu'(\nabla\|\nabla\phi_N\|) \cdot \nabla\phi_N}{4\pi G a_0}. \quad (11)$$

So, the Newtonian field  $-\nabla\phi_N$  becomes the only quantity necessary to determine at each radial step  $\rho_f$  and close the system of equations 6, 3 and 13 for a given boundary condition for the potential at the centre. The natural choice is to adopt  $\nabla\phi_N = 0$  at  $r = 0$  and then derive the radial profile of  $\nabla\phi_N$  from eq. 9 (see King 1966; Gunn & Griffin 1979).

For a cluster immersed in an external field, the argument of the function  $\nu$  is the magnitude of the total (internal plus external) gravitational field normalized to  $a_0$ . Because of the vectorial nature of the acceleration and of the different symmetry of the internal and external acceleration field, the magnitude of the total acceleration varies with the angle with respect to the direction of the external acceleration. This breaks the spherical symmetry of the system whose density/potential contours will be elongated. This introduces an inconsistency with the distribution function adopted in eq. 4. Indeed, while the energy remains an integral of motion regardless of the system geometry, the angular momentum magnitude  $L$  is not conserved in a non-spherical system. However, in slightly flattened potentials, say with axis ratios  $\gtrsim 0.9$ ,  $L$  is conserved within a few percent (Binney & Tremaine 2008, sect. 3.2.2, pag. 163). As we will see below (Sect. 2.2), our models are in fact slightly flattened, so we neglect this issue.

The outer boundary condition for the MOND and Newtonian gravitational fields are, respectively,

$$\lim_{r \rightarrow \infty} \nabla\phi^M = -\mathbf{a}_{\text{ext}}^M,$$

where  $\mathbf{a}_{\text{ext}}^M$  is the MOND external field, and

$$\lim_{r \rightarrow \infty} \nabla\phi_N = -\mathbf{a}_{\text{ext}}^N,$$

where  $\mathbf{a}_{\text{ext}}^N$  is the Newtonian external field.

It is convenient to define the internal gravitational potentials  $\psi_M$  and  $\psi_N$ , such that

$$\nabla\psi_M = \nabla\phi_M + \mathbf{a}_{\text{ext}}^M$$

and

$$\nabla\psi_N = \nabla\phi_N + \mathbf{a}_{\text{ext}}^N.$$

In order to account for the external field effect, in all the equations of this section we must replace  $\nabla\phi_M$  with  $\nabla\psi_M - \mathbf{a}_{\text{ext}}^M$  and  $\nabla\phi_N$  with  $\nabla\psi_N - \mathbf{a}_{\text{ext}}^N$ . Remarkably, as pointed out by Milgrom (2010),  $\mathbf{a}_{\text{ext}}^M$  drops from the equation for the internal potential  $\psi_M$ , which thus depends on  $\mathbf{a}_{\text{ext}}^M$ , but not on  $\mathbf{a}_{\text{ext}}^M$ . In practice, the QUMOND internal field  $\psi_M$  can be obtained by solving, with boundary condition  $\nabla\psi_M \rightarrow 0$  at infinity, the equation

$$\nabla^2\psi_M = 4\pi G\rho_f \quad (12)$$

where

$$\rho_f = \nu\rho + \frac{\nu'(\nabla\|\nabla\psi_N - \mathbf{a}_{\text{ext}}^N\|) \cdot (\nabla\psi_N - \mathbf{a}_{\text{ext}}^N)}{4\pi G a_0} \quad (13)$$

(see Milgrom 2010; Chae & Milgrom 2022). As usual,  $\psi_N$  can be obtained by solving

$$\nabla^2\psi_N = 4\pi G\rho, \quad (14)$$

with standard boundary conditions.

The internal potential  $\psi_M$  is not spherically symmetric, but will maintain a symmetry with respect to the direction of the external field. So, it is possible to express all the involved quantities (density, potential, velocity dispersions, etc.) as functions of the spherical polar coordinates  $r$  and  $\theta$ , where  $0 < \theta < \pi$  is the angle formed with the positive  $z$  axis, which is taken to have the same direction and orientation of the external field, while there is no dependence on the azimuthal coordinate  $\phi$ . We write the Newtonian and MOND potentials and densities as combinations of  $N$  Legendre polynomials

$$\begin{aligned} \psi &= \sum_{k=0}^N u_k(r) P_k(\theta), \\ \rho &= \sum_{k=0}^N g_k(r) P_k(\theta), \end{aligned} \quad (15)$$

where the functions  $u_k$  and  $g_k$  can be found by applying Laplace's equation and the variation of constant formula (see Prendergast & Tomer 1970; Wilson 1975), so that

$$u_0 = \psi_0 + 4\pi G \left( \int_0^r r g_0 dr - \frac{1}{r} \int_0^r r^2 g_0 dr \right), \quad (16)$$

and

$$u_k = -\frac{4\pi G}{2k+1} \left( r^k \int_r^\infty r^{1-k} g_k dr + r^{-1-k} \int_0^r r^{k+2} g_k dr \right), \quad (17)$$

where

$$g_k = \frac{2k+1}{2} \int_0^\pi \rho P_k \sin\theta d\theta \quad (18)$$

and  $\psi_0$  is the central potential. The same coefficients for QUMOND models can be calculated by replacing  $\rho$  with  $\rho_f$  in eq.s 18.

The gradient of the internal Newtonian potential is therefore

$$\begin{aligned} \nabla\psi_N &= \left( \sum_{k=0}^N \frac{du_k}{dr} - \|\mathbf{a}_{\text{ext}}^N\| \cos\theta \right) \hat{\mathbf{e}}_r \\ &+ \left( \sum_{k=0}^N \frac{u_k}{r} \frac{dP_k}{d\theta} - \|\mathbf{a}_{\text{ext}}^N\| \sin\theta \right) \hat{\mathbf{e}}_\theta. \end{aligned}$$

The model is computed iteratively, starting from  $N = 0$  (for which the model is spherical,  $g_0 = \rho$  and eq. 16 is simply the canonical Poisson equation in its integral form). The density profile of the  $N = 0$  model is then used to compute the fake density in the  $(r, \theta)$  plane (from eq. 13), the QUMOND potential (eq. 3), the actual density and velocity dispersions (eq. 6), the high-order asymmetric components  $g_k$  and  $u_k$  (eq.s 18), and a new model is computed. We found that  $N = 5$  provides reasonably stable models with only negligible differences with respect to higher-order models. Note that a symmetric Newtonian potential  $\psi_N$ , because of the presence of the external field, produces an asymmetric fake density profile along the direction of the external field. So, the density distributions of subsequent iterations are shifted

along this direction. The updated density distribution is then shifted to bring the system centre to the origin of the axes and used as input to construct the models of the next iteration. The density profiles of different steps are then compared and a new iteration is started if the average variation exceeds 0.1% of the central density.

The model is then projected in the plane of the sky and the observational quantities (projected density  $\Sigma$  and velocity dispersions along the line of sight  $\sigma_{\text{LOS}}$ , projected radial  $\sigma_R$  and tangential  $\sigma_T$  directions) are calculated.

In practice, it is convenient to express all quantities as dimensionless by normalizing the densities to the central value  $\rho_0$  of  $\rho$ , the radii and the potential to characteristic values ( $r_c$  and  $\sigma_K^2$ ) and the external acceleration to  $a_0$ :

$$\begin{aligned} \tilde{\rho} &= \rho/\rho_0, & \tilde{\rho}_f &= \rho_f/\rho_0, \\ \tilde{r} &= r/r_c, & W &= -\psi/\sigma_K^2, \\ \tilde{a} &= |\mathbf{a}_{\text{ext}}^{\text{N}}|/a_0, & \tilde{r}_a &= r_a/r_c. \end{aligned} \quad (19)$$

The shape of each QUMOND model is completely defined by five parameters: the central dimensionless potential  $W_0$ , the parameter  $\xi = \sigma_K^2/(a_0 r_c)$ , the strength of the external acceleration  $\tilde{a}$  and the anisotropy radius  $\tilde{r}_a$ , and the cluster mass  $M$ , which determines both  $\sigma_K^2$  and  $r_c$  through the relations

$$r_c = \sqrt{\frac{4\pi GM}{9I\xi a_0}}, \quad (20)$$

$$\sigma_K^2 = \sqrt{\frac{4\pi GM\xi a_0}{9I}}, \quad (21)$$

and

$$\rho_0 = \frac{9\sigma_K^2}{4\pi G r_c^2}, \quad (22)$$

where

$$I = 2\pi \int_0^\pi \int_0^\infty \tilde{r}^2 \sin\theta \tilde{\rho} d\tilde{r} d\theta$$

(see also Sollima & Nipoti 2010).

In appendix we report more details about the computation of the models (Appendix A) and of the external acceleration (Appendix B).

## 2.2 Model properties

To illustrate the characteristics of our models, we start with two reference sets of parameters corresponding to an isotropic and a maximally radially anisotropic model. Both reference models have a mass of  $10^5 M_\odot$ , a central dimensionless potential  $W_0 = 5$ , a MOND parameter  $\xi = 1$  and are immersed in a uniform external field with magnitude  $\tilde{a} = 1$ . So, the only varying parameter is  $\tilde{r}_a$  which is obviously set to  $\infty$  in the isotropic case and to  $\tilde{r}_{a,\text{min}} = 1.3$  in the anisotropic case. This value corresponds to a value of the Fridman-Poliachenko index  $\zeta$  lower than 1.7, which is the maximum value for which an anisotropic system remains stable against bar instability (Nipoti, Ciotti, & Londrillo 2011). We recall that  $\zeta$  is a *global* measure of anisotropy, defined as the the ratio of kinetic energy in radial and tangential motions:

$$\zeta = \frac{2T_r}{T_t} = \frac{2 \int_0^\pi \int_0^\infty \tilde{r}^2 \sin\theta \tilde{\rho} \sigma_r^2 d\tilde{r} d\theta}{\int_0^\pi \int_0^\infty \tilde{r}^2 \sin\theta \tilde{\rho} \sigma_t^2 d\tilde{r} d\theta} \quad (23)$$

(Fridman & Poliachenko 1984). In the following, we will quantify the degree of *local* anisotropy using the parameter

$$\beta = 1 - \frac{\sigma_t^2}{2\sigma_r^2}$$

for the three-dimensional structure of the system, and, when dealing with projected quantities, its analogue

$$\beta'' = 1 - \left( \frac{\sigma_T}{\sigma_R} \right)^2,$$

where  $\sigma_R$  and  $\sigma_T$  are, respectively, the radial and tangential components in the plane of the sky of the velocity dispersion integrated along the line of sight (Sollima et al. 2015).

In the top panels of Figs 1 and 2 the maps of density, potential, velocity dispersion and anisotropy in the meridional plane ( $x, z$ ) (with the positive  $z$  axis with the same direction and orientation as the external field) are shown, for the isotropic and anisotropic models, respectively. It can be seen that both models are almost spherical. A zoom of the above profiles along the  $x$  and the  $z$  axes inside the core is shown in the bottom panels of the same figures. Here the small ( $z_{\text{peak}} \sim 0.1 r_c$ ) shift of the peak density toward the direction of the external field is noticeable. The profiles of other quantities along the  $x$  and  $z$  axes are almost indistinguishable. As expected, in the anisotropic model the  $\beta$  parameter progressively increases toward the outer region of the system.

Fig. 3 shows the flattening ( $q$ ) and asymmetry ( $e$ ) profiles, defined as

$$\begin{aligned} q &= 1 - x/z_+, \\ e &= 1 - z_-/z_+, \end{aligned}$$

where  $x$ ,  $z_-$  and  $z_+$  are the distances from the density peak of a given density level along the  $x$  axis, and along the negative and positive branches of the  $z$  axis, respectively. It can be noted that there is an inversion of the trends of these quantities moving from the centre to the outer part of the system. In particular, in the very central region (at  $r < 0.5 r_c$ ) the system is elongated in the direction of the external field, but outside this region the trend inverts reaching very small ( $e, q < 0.1$ ) flattening and asymmetry in the opposite direction. The same trend is magnified in the anisotropic model, never reaching significant levels of flattening and anisotropy. On the basis of the above evidence of small deviations from spherical symmetry, we can consider the angular momentum as a quasi-conserved quantity and safely adopt eq. 4 also for QUMOND models (see Sect. 2.1).

The deviations from central symmetry are even smaller when considering projected quantities. In Figs 4 and 5 the projected density and the three components of the velocity dispersion are shown along the  $X$ ,  $Z_-$  and  $Z_+$  directions. Here,  $X$ ,  $Z_-$  and  $Z_+$  are the equivalent of the 3D distances  $x$ ,  $z_-$  and  $z_+$ , but projected into the plane of the sky assuming a line of sight orthogonal to  $z$  to maximize the flattening and the asymmetry. Note that all profiles are extremely similar with differences of the order of 0.1 dex in the logarithmic density and  $< 0.1$  km/s in the velocity dispersion for both isotropic and anisotropic models. In this case, the model appears slightly elongated in the direction of the external field.

We plot in Fig. 6 the projected density and velocity dispersion of the isotropic reference model by changing one parameter at time. Here it can be visualized that  $W_0$  mainly affects

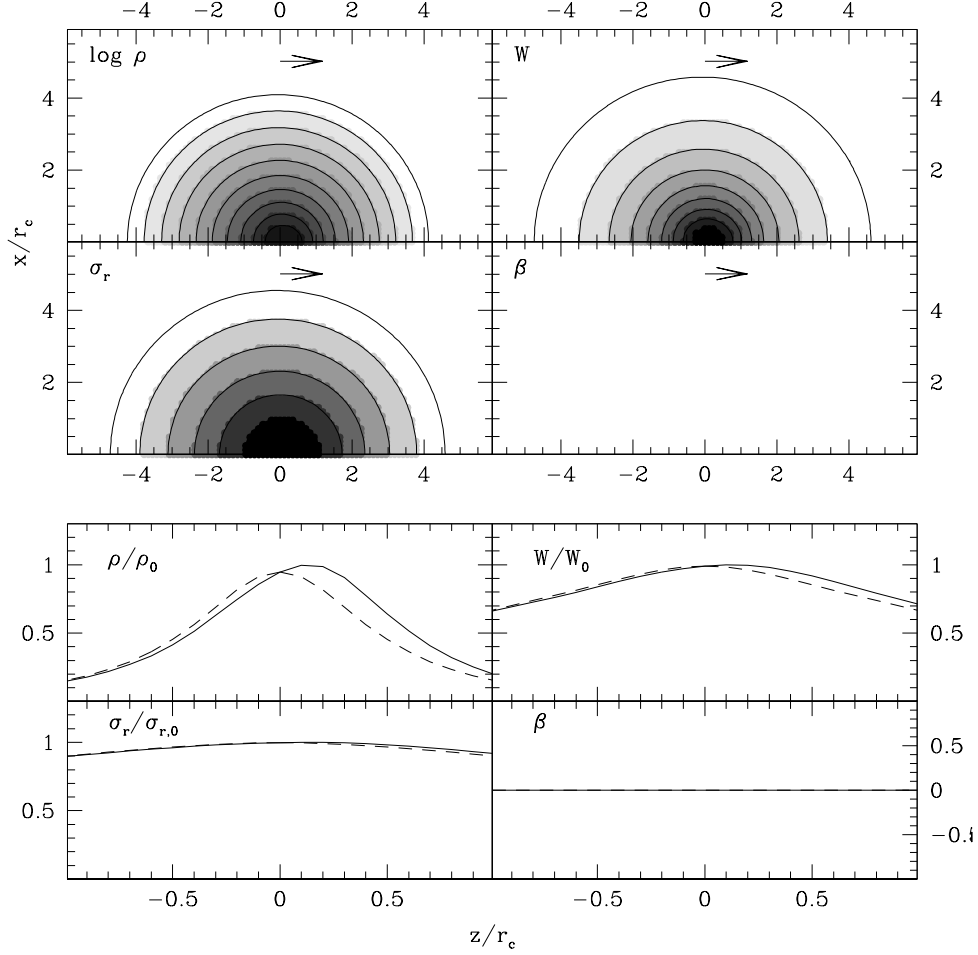


**Figure 1.** Properties of the reference isotropic model (from top to bottom). First row: maps of the logarithmic density (left panel) and dimensionless potential (right panel). Second row: radial velocity dispersion (left panel) and anisotropy parameter (right panel). Darker contours indicate larger values in steps of 10% of the central value. The direction of the external acceleration is shown by an arrow. Third row: central density (left panel) and potential (right panel) profiles, along (solid lines) and orthogonal to (dashed lines) the direction of the external field. Fourth row: radial velocity dispersion (left panel) and anisotropy parameter (right panel; here  $\beta = 0$  everywhere) profiles, along (solid lines) and orthogonal to (dashed lines) the direction of the external field.

the model concentration (as in all canonical Newtonian models; see [King 1966](#); [Gunn & Griffin 1979](#)) with models with high  $W_0$  asymptotically approaching the isothermal sphere. The parameter  $\xi$  is instead an indicator of the internal acceleration field, and therefore determines the contribution of internal gravity to keep the system in the MOND regime. Indeed, models with large values of  $\xi$  progressively approach their Newtonian equivalent. The same occurs for the  $\tilde{a}$  parameter for the external acceleration: the stronger the external field, the closer the system to the Newtonian model. Finally, the parameter  $\tilde{r}_a$  determines the degree of anisotropy, with lower values of  $\tilde{r}_a$  corresponding to elongation of the velocity ellipsoids occurring at smaller distance from the centre.

A different experiment is shown in [Fig. 7](#). Here the projected density profile of the QUMOND isotropic reference

model is fit with a Newtonian model, and the Newtonian and MOND projected velocity dispersion profiles are compared. It is apparent that the QUMOND model predicts a larger velocity dispersion across the entire extent of the system. As already discussed in [Sect. 1](#), this is a consequence of the stronger gravitational field predicted by MOND in regimes of low accelerations (eq. 1). In MOND all cluster stars able to cross the low-acceleration region need more kinetic energy with respect to the classical Newtonian gravitation law. Any region of the cluster contains a fraction of these stars, so the velocity dispersion is inflated at all radii.

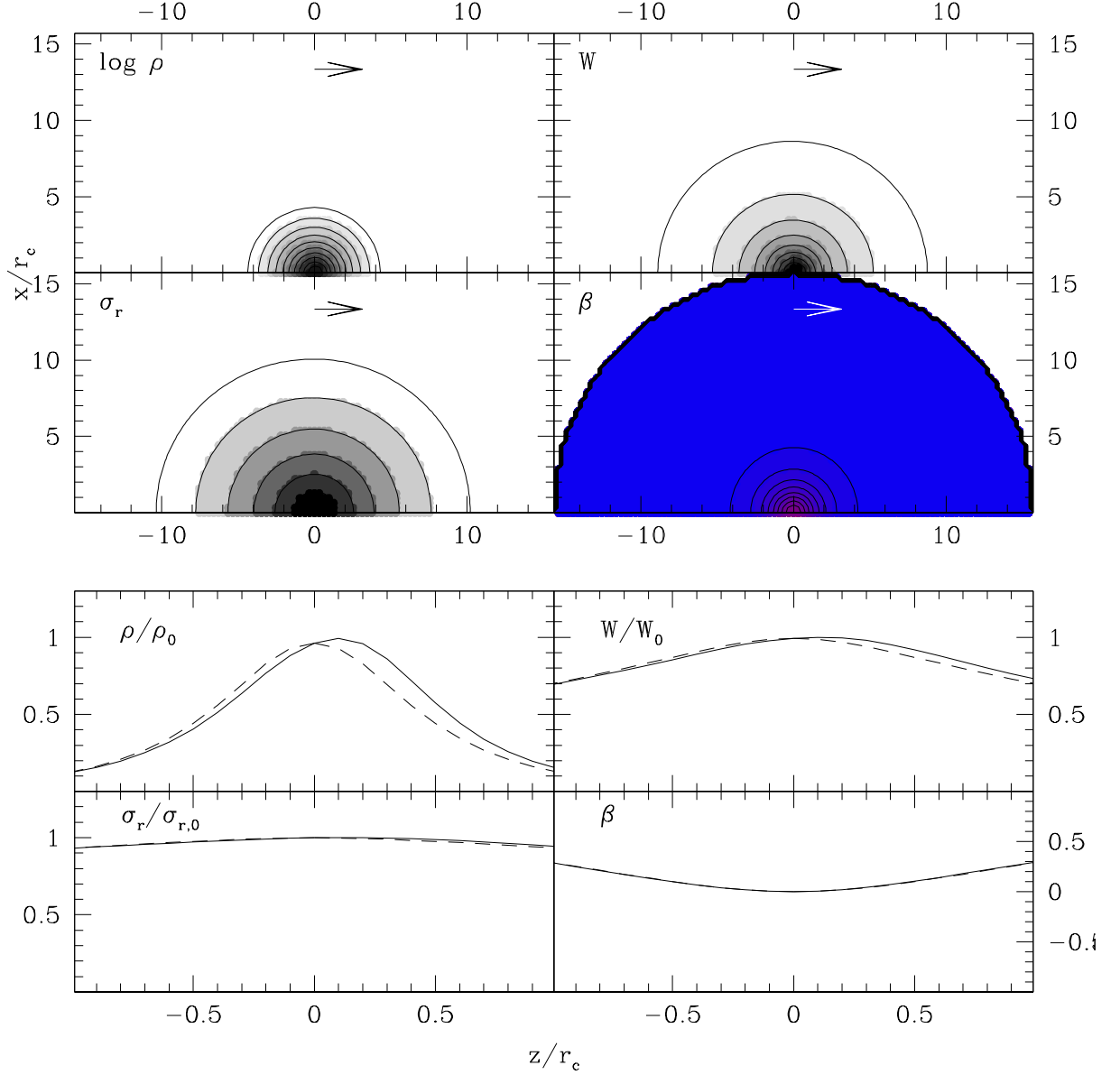


**Figure 2.** Same as Fig. 1, but for the anisotropic reference model. In the map of the anisotropy parameter, colors range from red (more isotropic) to blue (more radially anisotropic).

### 3 OBSERVATIONAL DATA

#### 3.1 GC data

Among the 160 Galactic GCs, only a small subsample can be useful for our analysis.

The selection has been made on the basis of three different criteria: *i*) the absence of significant rotation, *ii*) the availability of accurate MFs sampled down to the least massive

stars ( $m \sim 0.1M_\odot$ ), close to the hydrogen burning limit, *iii*) the availability of a significant number of accurate kinematic data (proper motions and line-of-sight velocities).

The first criterion is based on the fact that our models lack a treatment of internal rotation. Note that in some GCs rotation is significant, and the rotation and pressure supports are comparable (Sollima, Baumgardt, & Hilker 2019). So, we first exclude all those GCs which are classified as "signifi-

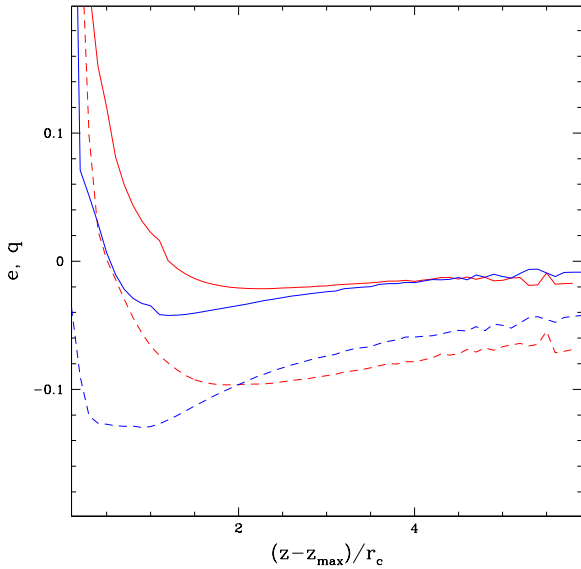


**Figure 3.** Flattening (blue lines) and asymmetry (red lines) profiles for the isotropic (solid lines) and anisotropic (dashed lines) reference models.

cant" or "uncertain" rotators in any of the compilations of Sollima, Baumgardt, & Hilker (2019) and Vasiliev & Baumgardt (2021).

The second criterion is based on the approach we will adopt in Sect. 4 to compute the consistency of our best-fit models with observations. Indeed, we need to compare our dynamical  $M/L$  with those obtained from the comparison of the stellar population synthetically derived from stellar models. A fundamental input of these models is the MF which needs to be well sampled across the entire extent covered by each GC, including the very low-mass stars contributing to the cluster mass more than to the light. We adopted the MF measurements by Baumgardt et al. (2023) and restricted our sample to those GCs with a lower mass limit  $m < 0.26M_{\odot}$ .

The third criterion is based on the statistical robustness of the derived  $M/L$  and of the constraint on the anisotropy parameters. We limit our analysis to GCs with at least 50 radial velocities and 50 proper motions with the required accuracy (see Sect. 3.3).

After the application of the above criteria, we selected a sample of 18 GCs. They are listed in Table 1. They span a heliocentric distance range  $1.8 < R_{\odot}/\text{kpc} < 18.5$  and a Galactocentric distance range  $2.5 < R_{GC}/\text{kpc} < 18.5$ .

In Fig. 8, the 160 GCs of the Baumgardt & Hilker (2018) sample are plotted in the  $\log(a_{int,hm}^N/a_0)$  vs.  $\log a_{ext}^N/a_0$  plane. Here,

$$a_{int,hm}^N = \frac{GM}{2r_h^2}$$

is the Newtonian internal acceleration magnitude of the cluster measured at the half-mass radius  $r_h$  and  $a_{ext}^N$  is the external acceleration magnitude calculated as described in Appendix B (eq. B2). Clusters distribute in this plane along a

**Table 1.** Properties of the Newtonian and QUMOND best-fit models. Column 1: name of the GC. Column 2: minimum  $V$ -band mass-to-light ratio (see Sect. 4.2). Columns 3 and 4:  $V$ -band mass-to-light ratio and probability (see Sect. 4.1) of the best Newtonian model. Columns 5 and 6:  $V$ -band mass-to-light ratio and probability of the best QUMOND model. Mass-to-light ratios are in solar units.

NGC	$(M/L_V)_{min}$	Newtonian		QUMOND	
		$M/L_V$	$P$	$M/L_V$	$P$
288	0.988	2.931	1.000	1.400	0.997
1261	0.811	1.896	1.000	1.097	0.965
1851	0.887	2.132	1.000	2.069	1.000
4590	1.187	2.960	1.000	1.883	0.984
4833	0.872	1.348	1.000	1.069	0.844
5024	1.232	2.028	1.000	0.927	0.005
5897	1.329	2.393	1.000	1.339	0.591
6101	1.329	2.568	1.000	1.386	0.640
6121	1.059	1.895	1.000	1.549	0.977
6171	0.953	2.078	1.000	1.518	1.000
6254	0.900	1.749	1.000	1.485	0.983
6352	0.943	2.067	0.999	3.198	1.000
6362	0.868	1.965	1.000	1.274	1.000
6366	0.720	1.564	1.000	1.077	0.994
6496	1.151	1.643	0.981	1.270	0.754
6723	0.927	2.232	1.000	1.697	1.000
6779	0.844	3.147	1.000	3.063	1.000
6838	0.725	1.207	1.000	1.191	1.000

diagonal, because of the well-known Galactocentric distance-size relation (van den Bergh, Morbey, & Pazder 1991). It is apparent that all GCs with both  $a_{int,hm}^N < a_0$  and  $a_{ext}^N < a_0$  are outside the region where all the selection criteria are satisfied. Indeed, they are too far to have accurate proper motions and a properly sampled MF. Instead, those matching all the criteria occupy a region shared by many GCs between  $0.32 < \tilde{a} < 4.88$ .

### 3.2 Surface density profiles

We account for the structural properties of the observed GCs, considering circularized surface density profiles. In particular, we adopt the surface density profiles of Mocchi et al. (2013) when available and those of Trager, King, & Djorgovski (1995) otherwise. For six GCs (NGC4833, NGC6101, NGC6352, NGC6362, NGC6496 and NGC6838) we calculated profiles using the ACS HST catalogs of Anderson et al. (2008) for the cluster cores and those of Stetson et al. (2019) for the outskirts. For this purpose, we converted F606W HST magnitudes into Johnson ones using the transformations of Sirianni et al. (2005), and selected stars along the main sequence in the common magnitude interval  $12 < V < 19$  where the photometric completeness is expected to be  $> 90\%$ . The surface density has been calculated by counting stars in circular annuli and dividing by the correspondent area.

### 3.3 Proper motions and radial velocities

To account for the kinematic properties of the observed GCs, we rely mainly the proper motions provided by the 3rd data release of the Gaia survey (Gaia Collaboration et al. 2021) and the database of radial velocities collected by Baumgardt



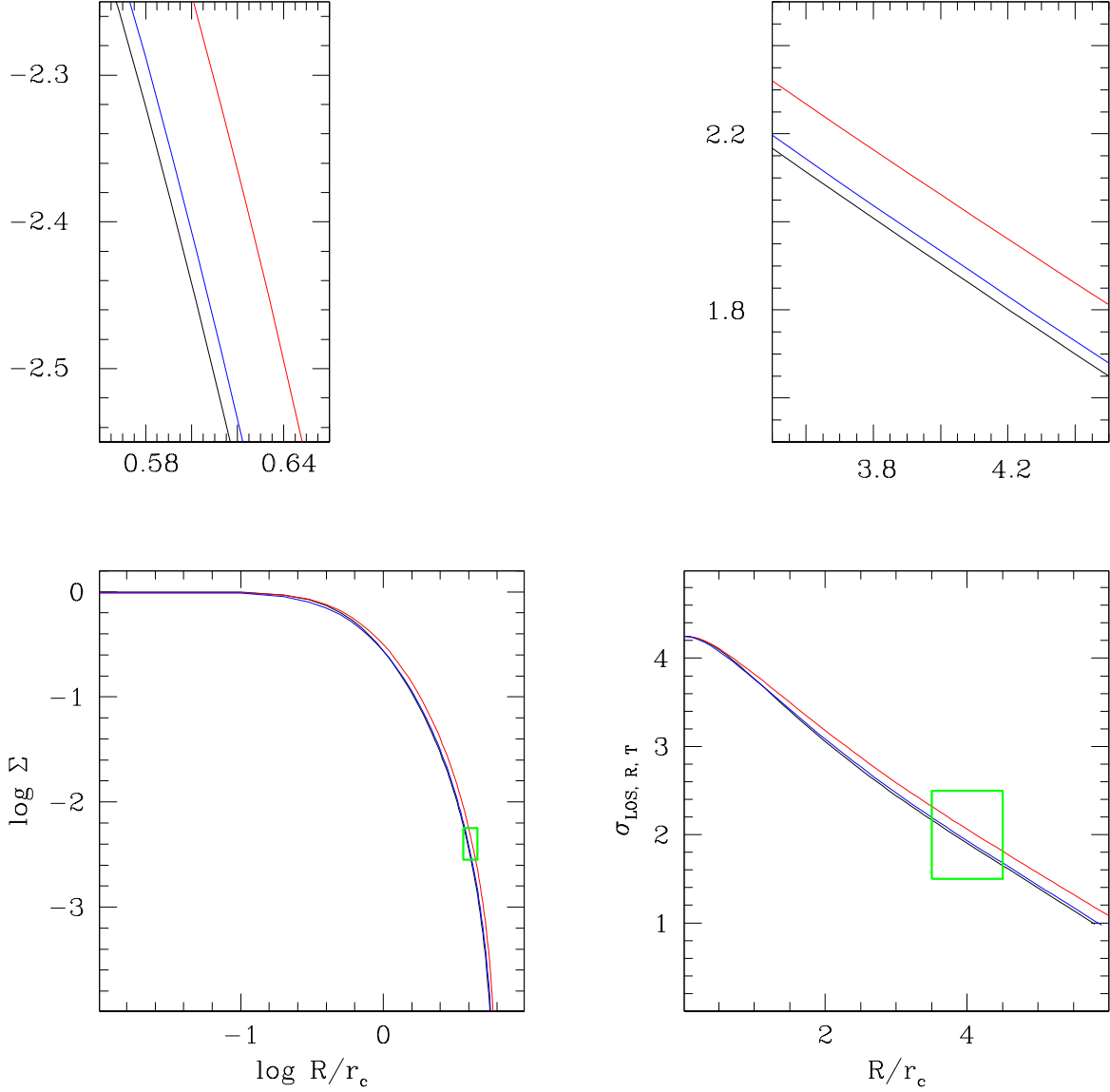


**Figure 4.** Projected density (lower left panel) and velocity dispersion (lower right panel) profiles of the isotropic reference model, along the positive (black curves) and negative (red curves) branches of the  $Z$  axis, and along the  $X$  axis (blue curves). We recall that the positive  $Z$  axis is parallel to and oriented as the external field (see text). The upper panels show zooms of the green regions marked in the corresponding bottom panels.

& Hilker (2018) using a compilation of high-resolution spectroscopic data properly aligned. We cross-matched the two data sets in order to obtain a single catalog per cluster containing all the three components of the velocities.

From this catalog we want to extract a selection of sufficiently accurate kinematic measurements for a subsample of bona-fide cluster members. For this purpose, we find it convenient to use as reference a Newtonian dynamical model of the cluster. We thus fit the surface density profiles (Sect. 3.2) of each cluster with an isotropic ( $r_a/r_c = \infty$ ) Newtonian Gunn & Griffin (1979) model providing a normalized veloc-

ity dispersion ( $\tilde{\sigma}_{v,i}^2$  and  $\tilde{\sigma}_{\mu,i}^2$  for radial velocities and proper motions, respectively) at the projected radius of each star  $R_i$ .

To obtain the corresponding velocity dispersions in physical units  $\sigma_{v,i} \equiv \sigma_v(R_i)$  and  $\sigma_{\mu,i} \equiv \sigma_\mu(R_i)$ , we need two scaling factors ( $\sigma_{v,0}$  and  $\sigma_{\mu,0}$ ) such that  $\sigma_{v,i} = \sigma_{v,0}\tilde{\sigma}_{v,i}$  and  $\sigma_{\mu,i} = \sigma_{\mu,0}\tilde{\sigma}_{\mu,i}$ . The relation between the two scaling factors is

$$\sigma_{v,0} = 4.74 \left( \frac{R_\odot}{\text{kpc}} \right) \left( \frac{\sigma_{\mu,0}}{\text{mas/yr}} \right) \text{ km s}^{-1}, \quad (24)$$

where  $R_\odot$  is the cluster distance. Throughout this work, we

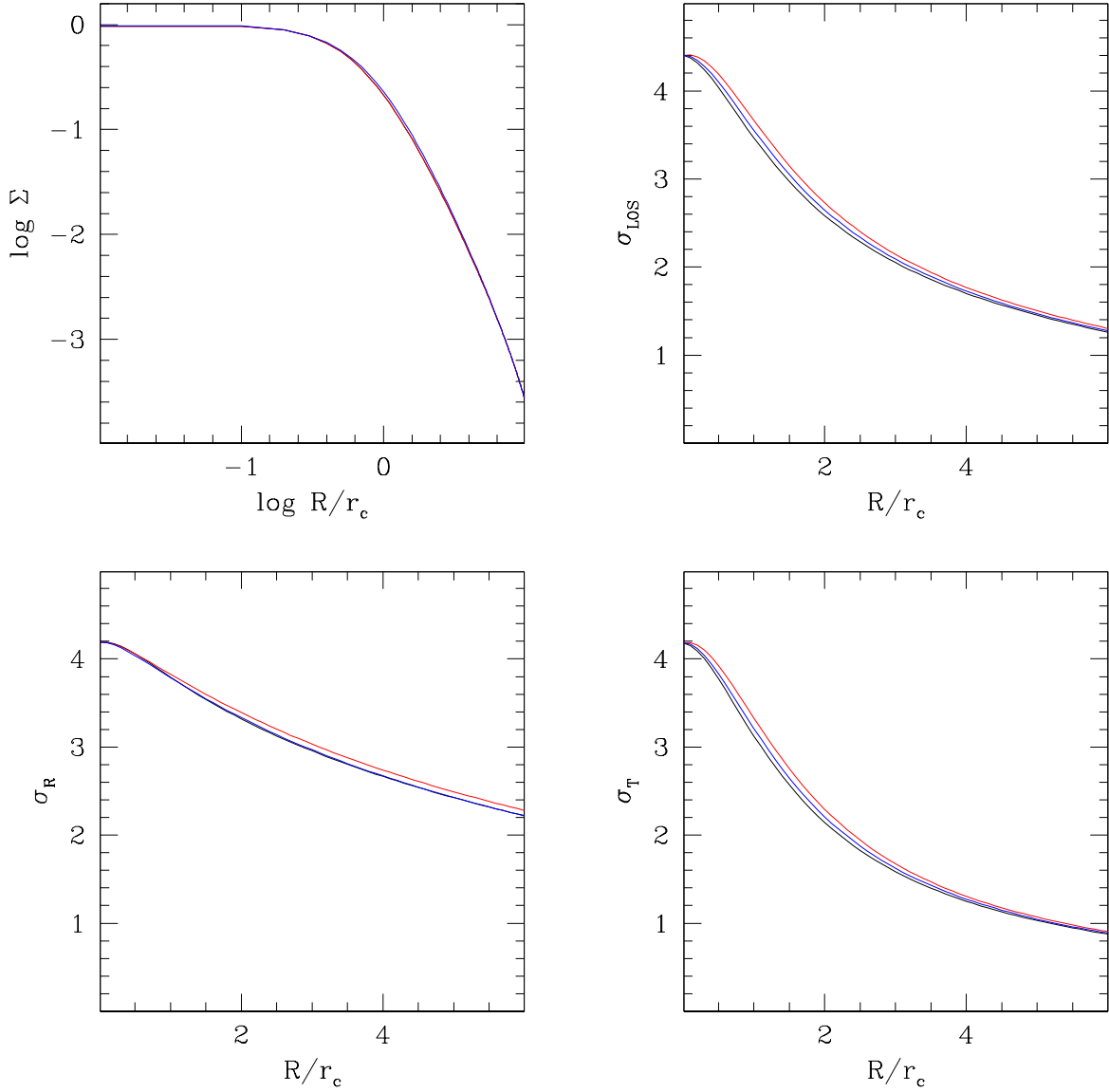


**Figure 5.** Same as the lower panels of Fig. 4, but for the anisotropic reference model. Here, given that the model is anisotropic, we show separately the line-of-sight, and plane-of-the-sky radial and tangential velocity dispersion profiles.

adopt the distances from [Baumgardt & Vasiliev \(2021\)](#), so in the following  $\sigma_{v,0}$  is left as a free parameter of the model, while  $\sigma_{\mu,0}$  is obtained from  $\sigma_{v,0}$  using eq. 24.

The best-fitting isotropic Newtonian model is found by maximizing the likelihood

$$\ln L_{\Sigma} = -\frac{1}{2} \sum_{j=1}^M \left( \frac{\log \Sigma_{\text{obs},j} - \log \tilde{\Sigma}(R_j) - \log \Sigma_0}{\delta \log \Sigma_{\text{obs},j}} \right)^2, \quad (25)$$

where  $\Sigma_{\text{obs},j}$  is the observed surface density at radius  $R_j$ ,  $\delta \log \Sigma_{\text{obs},j}$  is the uncertainty on  $\log \Sigma_{\text{obs},j}$ ,  $\tilde{\Sigma}(R)$  is the normalized model's surface density at projected radius  $R$  and  $\Sigma_0$

is the central surface density of the model, which is left as a free parameter.

Then, we fit iteratively the mean cluster velocity components ( $\langle \mu_{\alpha}^* \rangle$ ,  $\langle \mu_{\delta} \rangle$  and  $\langle v \rangle$ ) starting from the initial guesses of [Vasiliev & Baumgardt \(2021\)](#), together with the scaling factor  $\sigma_{v,0}$ , selecting those providing the maximum likelihood defined as

$$\ln L_{kin} = \ln L_v + \ln L_{\mu},$$

$$\ln L_v = \sum_{i=1}^N \ln L_{v,i},$$

$$\ln L_{v,i} = -\frac{1}{2} [\delta_{v,i}^2 + \ln s_{v,i}^2 + \ln(2\pi)],$$

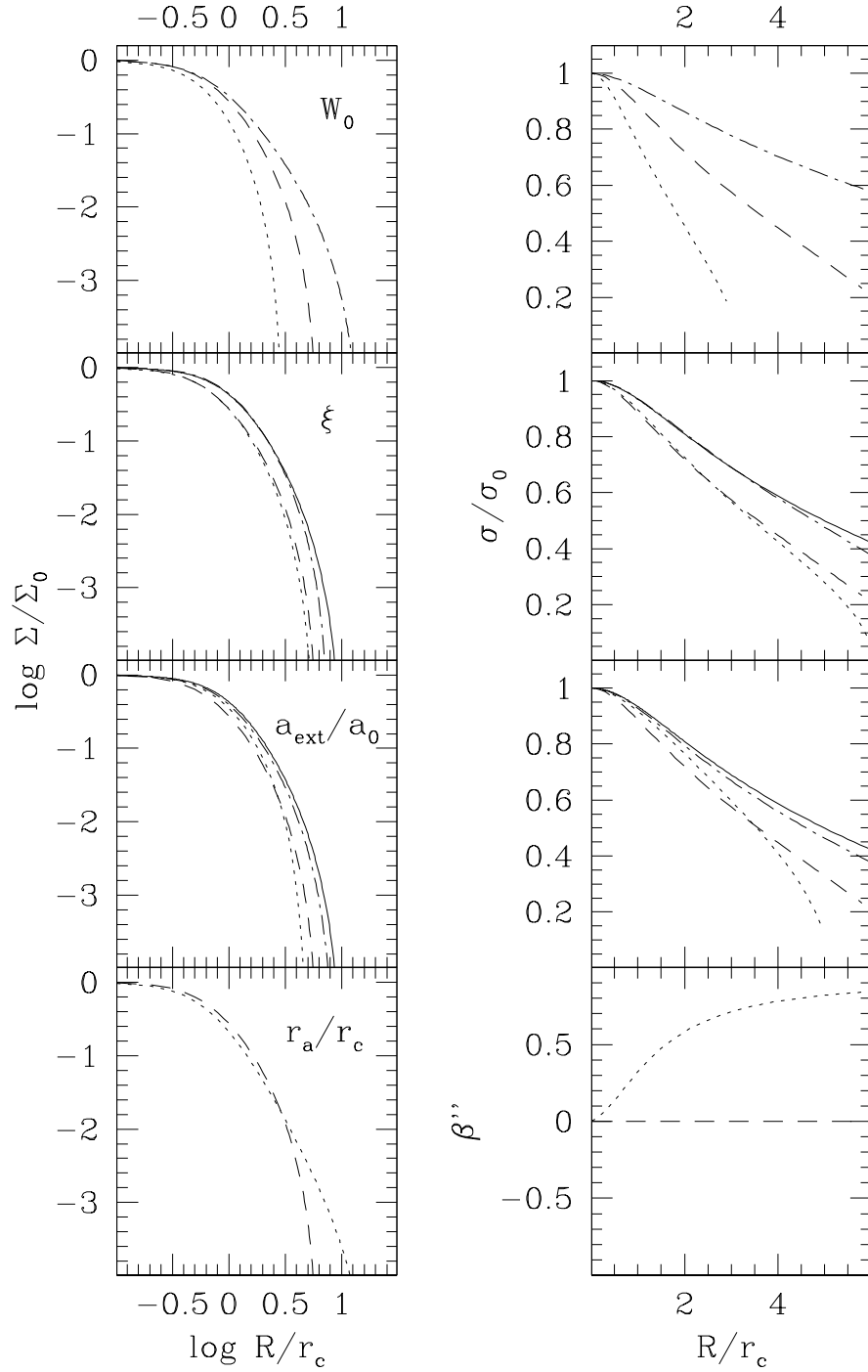


**Figure 6.** Projected density (left panels) and velocity dispersion (right panels) profiles of QUMOND models which are obtained from the isotropic reference model by varying one parameter at a time. From top to bottom:  $W_0 = 3, 5, 7$ ,  $\xi = 0.1, 1, 10$ ,  $\bar{a} = 0.1, 1, 10$  (marked in each panel with dotted, dashed and dot-dashed lines, respectively) and  $\bar{r}_a = 1.3, \infty$  (marked with dotted and dashed lines, respectively). In the panels relative to the parameters  $\xi$  and  $\bar{a}$ , the Newtonian model with the same value of  $W_0$  is also plotted with solid lines.

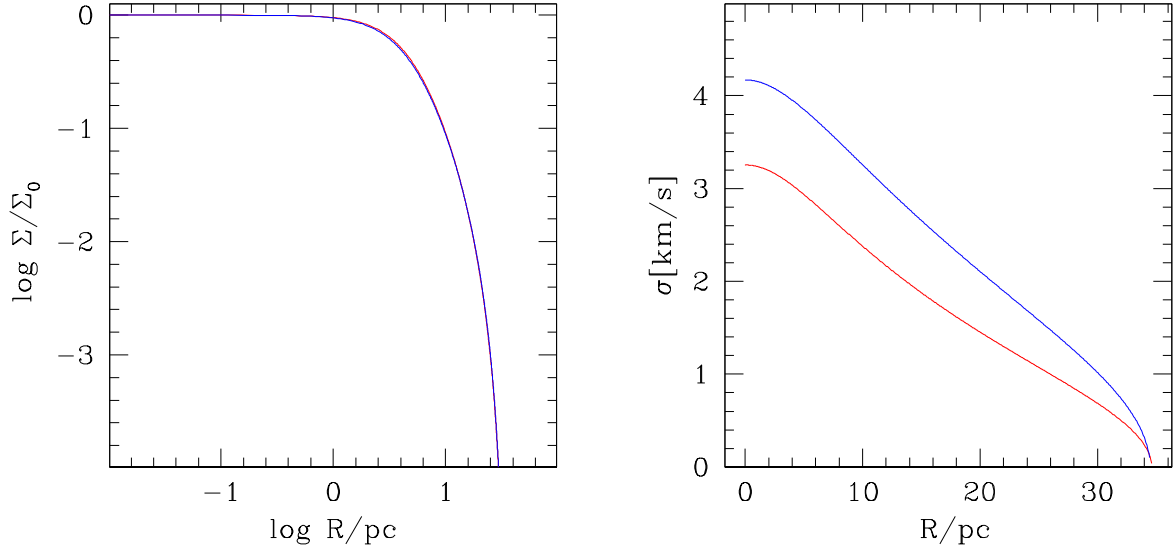


**Figure 7.** Projected density (left panel) and velocity dispersion (right panel) profiles of the QUMOND isotropic reference model (blue lines) and of the Newtonian model with the same projected density profile (red lines).

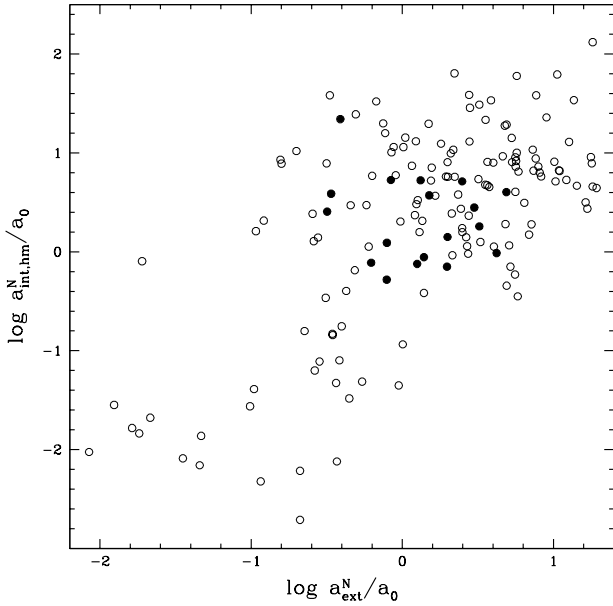


**Figure 8.** Location of the 160 GCs of the Baumgardt & Hilker (2018) database (open dots) in the  $\log(a_{int,hm}^N/a_0)$  vs.  $\log(a_{ext}^N/a_0)$  plane. The 18 GCs analysed in this paper are marked by full dots.

$$\begin{aligned} \ln L_\mu &= \sum_{i=1}^N \ln L_{\mu,i}, \\ \ln L_{\mu,i} &= -\frac{1}{2} [\delta X_i^2 + \delta Y_i^2 - 2\tilde{\varrho}_i \delta X_i \delta Y_i + \ln(1 - \tilde{\varrho}_i^2) + \ln(s_{\mu X,i}^2 s_{\mu Y,i}^2)] - \ln(2\pi), \end{aligned} \quad (26)$$

where

$$\begin{aligned} \delta X_i^2 &= \frac{(\mu_{\alpha,i}^* - \langle \mu_\alpha^* \rangle)^2}{(1 - \tilde{\varrho}_i^2) s_{\mu X,i}^2}, \\ \delta Y_i^2 &= \frac{(\mu_{\delta,i} - \langle \mu_\delta \rangle)^2}{(1 - \tilde{\varrho}_i^2) s_{\mu Y,i}^2}, \\ s_{\mu X,i}^2 &= \epsilon_{\mu\alpha,i}^2 + \sigma_{\mu,i}^2, \\ s_{\mu Y,i}^2 &= \epsilon_{\mu\delta,i}^2 + \sigma_{\mu,i}^2, \\ \tilde{\varrho}_i &= \frac{\varrho_{\alpha\delta,i} \epsilon_{\mu\alpha,i} \epsilon_{\mu\delta,i}}{s_{\mu X,i} s_{\mu Y,i}}, \\ \delta v_i^2 &= \frac{(v_i - \langle v \rangle)^2}{s_{v,i}^2}, \\ s_{v,i}^2 &= \epsilon_{v,i}^2 + \sigma_{v,i}^2. \end{aligned}$$

Here  $N$  is the number of bona-fide cluster members at the current iteration,  $\mu_{\alpha,i}^*$ ,  $\mu_{\delta,i}$  and  $v_i$  are the proper motions and radial velocity of the  $i$ th star,  $\epsilon_{\mu\alpha,i}$ ,  $\epsilon_{\mu\delta,i}$  and  $\epsilon_{v,i}$  are their respective uncertainties,  $\varrho_{\alpha\delta,i}$  is the correlation coefficient between  $\mu_{\alpha,i}^*$  and  $\mu_{\delta,i}$ . We adopted Powell's gradient descent algorithm (Powell 1964) to find the maximum likelihood in the considered 4-dimensional parameter space. At each iteration, we eliminated from the sample of bona-fide cluster members all those stars with velocity lying at more than  $5\sigma$  in the model's velocity distribution at their radius. The algorithm converges after  $\sim 10$  iterations, providing the systemic motion of the cluster ( $\langle \mu_\alpha^* \rangle$ ,  $\langle \mu_\delta \rangle$  and  $\langle v \rangle$ ) and the central scaling factor of radial velocity ( $\sigma_{v,0}$ ). This value has been converted, using eq. 24 and the distances provided by Baumgardt & Vasiliev (2021), into proper motion scaling factor  $\sigma_{\mu,0}$ , which we adopted as upper limit in proper motion uncertainty ( $\epsilon_{\mu,max} = \sigma_{\mu,0}$ ). The parallaxes of member stars have been also used to determine the systemic cluster parallax ( $\langle p \rangle$ ) and its dispersion ( $\sigma_p$ ).

All the Gaia proper motions of stars contained within the tidal radius of the best-fit Gunn & Griffin (1979) model have been selected. Among them, we selected for our final sample the stars  $i$  lying along the characteristic sequences of

the  $G$ , ( $G_{BP} - G_{RP}$ ) colour-magnitude diagram, *ii*) with a parallax contained within  $5\sigma_p$  from the mean systemic cluster parallax, *iii*) with  $\ln L_{\mu,i} > \ln L_{\mu,best} - 5$  (where  $L_{\mu,best} = \max_i L_{\mu,i}$ ), and *iv*) with  $\min(\epsilon_{\mu\alpha,i}, \epsilon_{\mu\delta,i}) < \epsilon_{\mu,max}$ . Of course, from eq. 24, it is apparent that proper motions and their associated errors are proportional to the cluster distance. So, the more distant is the target GC the larger will be its proper motion uncertainty. Consequently, criterion (*iv*) greatly reduces the number of suitable proper motions for distant clusters.

In the next steps (Sect. 4) we use separately the sample of  $N_v$  line-of-sight velocities of bona-fide members and the Gaia sample of proper motions for  $N_\mu$  stars selected according to the above criteria.

## 4 TECHNIQUE

In this Section, we describe how we derived for each cluster the dynamical  $M/L_V$  predicted by the two different gravitation theories and its minimum value independently derived from stellar evolution models.

### 4.1 Model fit and dynamical $M/L_V$

Proper motions have been corrected for perspective rotation using eq. 1 of Gaia Collaboration et al. (2018b) and eq.s 4 and 6 of van de Ven et al. (2006). The celestial coordinates (RA, Dec) have been converted into projected distances from the cluster centre using equation 1 of van de Ven et al. (2006) and adopting the centres of Baumgardt & Hilker (2018). The  $\alpha$  and  $\delta$  proper motions of each star have been converted into radial ( $\mu_R$ ) and tangential ( $\mu_T$ ) proper motions in the plane of the sky, relative to the cluster centre.

The models have been projected along the line of sight, taking into account that the model symmetry axis  $z$  (aligned with the external field, which points towards the Galactic centre) forms with the line of sight an angle

$$i = \cos^{-1} \left( \frac{\mathbf{R}_{GC} \cdot \mathbf{R}_\odot}{\|\mathbf{R}_{GC}\| \|\mathbf{R}_\odot\|} \right),$$

where  $\mathbf{R}_{GC}$  and  $\mathbf{R}_\odot$  are the vectors connecting the cluster to the Galactic centre and to the Sun, respectively. Given that the projections of the models in the plane of the sky deviate negligibly from circular symmetry (see Sect. 2.2), for comparison with the data we computed for the model the angle averaged profiles of the following quantities integrated along the line of sight: the surface density  $\Sigma(R)$ , the line-of-sight velocity dispersion  $\sigma_{LOS}(R)$ , and the radial  $\sigma_{\mu R}(R)$  and tangential  $\sigma_{\mu T}(R)$  components of the proper-motion dispersion, calculated using the cluster distance  $R_\odot$  (here  $R$  is the distance from the centre in the plane of the sky).

For both Newtonian and QUMOND models we defined a sequence of values of  $M$  and  $\tilde{r}_a^{-1}$  from 0 to  $\tilde{r}_{a,min}^{-1}$  in steps of 0.1, where  $\tilde{r}_{a,min}$  is such that  $\zeta \simeq 1.7$  (see Sect. 2.2). As in Sect. 3.3, the normalization factor of proper motions has been calculated separately and used only to calculate the contribution of anisotropy to the likelihood. Then, for each pair  $(M, \tilde{r}_a)$ , using a Powell's gradient descent algorithm (Powell 1964), we searched for the pair of values of parameters,  $(W_0, r_c)$  for Newtonian models and  $(W_0, \xi)$  for QUMOND

ones, that maximize the following likelihood:

$$\ln L = \ln L_\Sigma + \ln L_v + \ln L_\mu, \quad (27)$$

where  $\ln L_\Sigma$  is defined in eq. 25,

$$\begin{aligned} \ln L_v &= \sum_{i=1}^{N_v} \ln L_{v,i}, \\ \ln L_\mu &= \sum_{i=1}^{N_\mu} \ln L_{\mu,i}, \end{aligned} \quad (28)$$

and  $\ln L_{v,i}$  and  $\ln L_{\mu,i}$  are defined as in eq. 26, but with

$$\begin{aligned} \delta X_i^2 &= \frac{(\mu_{R,i} - \langle \mu_R \rangle)^2}{(1 - \tilde{q}_i^2) s_{\mu X,i}^2}, \\ \delta Y_i^2 &= \frac{(\mu_{T,i} - \langle \mu_T \rangle)^2}{(1 - \tilde{q}_i^2) s_{\mu Y,i}^2}, \\ s_{\mu X,i}^2 &= \epsilon_{\mu R,i}^2 + \sigma_{\mu R}^2(R_i), \\ s_{\mu Y,i}^2 &= \epsilon_{\mu T,i}^2 + \sigma_{\mu T}^2(R_i), \\ \tilde{q}_i &= \frac{\rho_{RT,i} \epsilon_{\mu R,i} \epsilon_{\mu T,i}}{s_{\mu X,i} s_{\mu Y,i}}, \\ \delta v_i^2 &= \frac{(v_i - \langle v \rangle)^2}{s_{v,i}^2}, \\ s_{v,i}^2 &= \epsilon_{v,i}^2 + \sigma_{LOS}^2(R_i), \end{aligned}$$

where  $\mu_{R,i}$  and  $\mu_{T,i}$  are, respectively, the radial and tangential proper motions of the  $i$ th star,  $\epsilon_{\mu R,i}$  and  $\epsilon_{\mu T,i}$  are the corresponding uncertainties, and  $\rho_{RT,i}$  is the correlation coefficient between  $\mu_{R,i}$  and  $\mu_{T,i}$ .

By marginalizing over  $\tilde{r}_a^{-1}$  we obtain the global likelihood for a given cluster mass  $M$ :

$$\mathcal{L}(M) = \int_0^{\tilde{r}_{a,min}^{-1}} L(M, \tilde{r}_a^{-1}) d\tilde{r}_a^{-1}.$$

Masses have been then divided by the cluster luminosity, derived using the absolute  $V$ -band magnitudes by Baumgardt, Sollima, & Hilker (2020) and the solar absolute  $V$  magnitude  $M_V = 4.84$  (Prša et al. 2016), to obtain the corresponding distribution of  $\mathcal{L}$  for  $M/L_V$ , which is then normalized and fitted with a Gaussian. The best fit of the data of NGC5024 with Newtonian and QUMOND models are shown in Fig. 9, as an example. The dynamical  $M/L_V$  of our sample of GC are reported in Table 1.

### 4.2 Minimum $M/L_V$

The goal of this paper is to compare the dynamical  $M/L_V$  of our GCs sample with a dynamics-independent estimate, to test the validity of the Newtonian and QUMOND theories of gravitation. In particular, it is important to estimate an observationally inferred minimum  $M/L_V$  of the GC, independent of kinematics: as pointed out in the Introduction, for a gravitational theory to be acceptable, the dynamical  $M/L_V$  predicted by the theory must not be lower than this minimum value. Thus the estimate of the minimum  $M/L_V$  is a fundamental piece of the present investigation.

A viable option is provided by the  $M/L_V$  predicted by stellar evolution models. Indeed, each cluster star contributes to both mass and luminosity in a different way according to its initial mass and evolutionary stage. As a first step, we choose

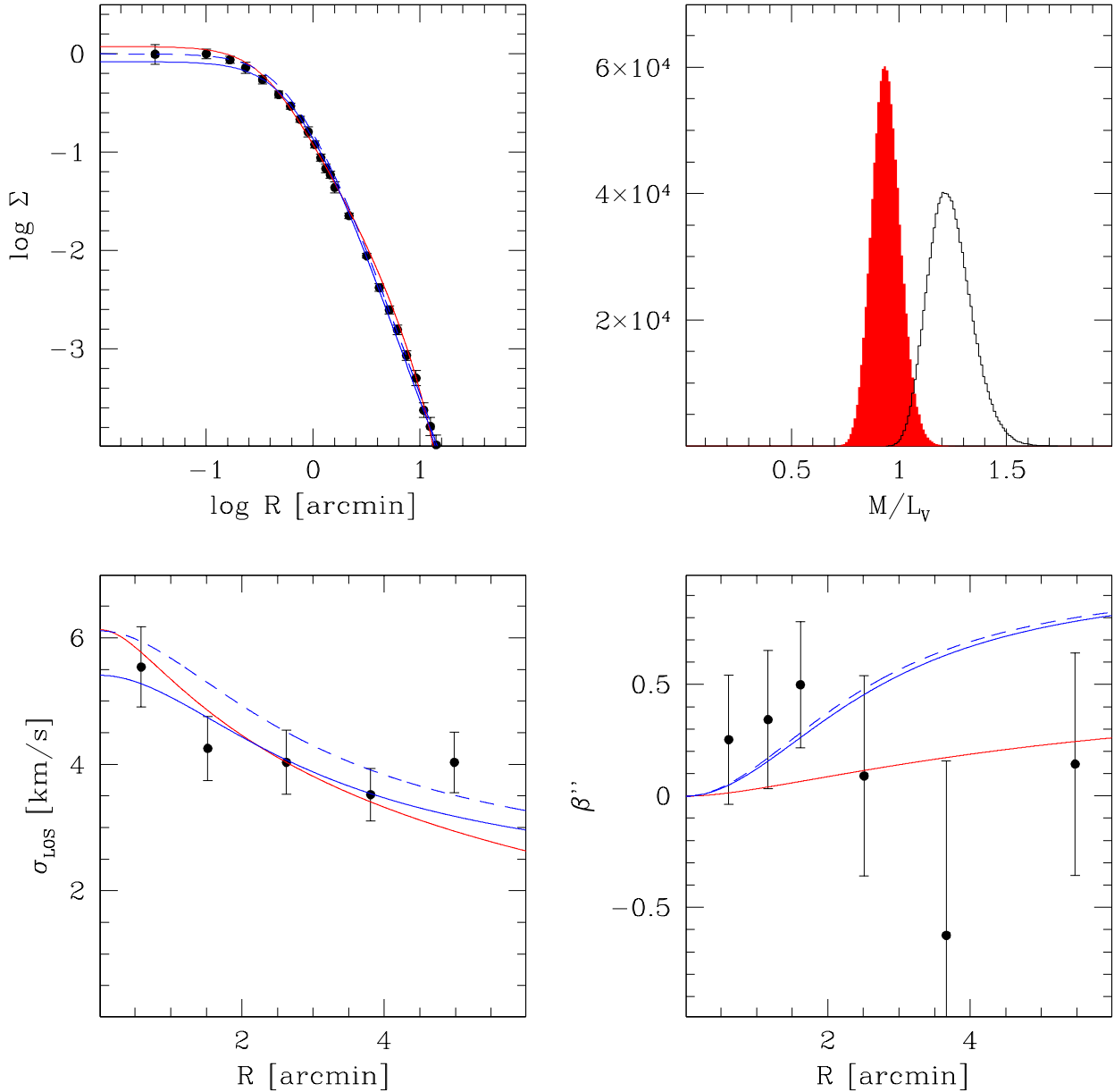


**Figure 9.** Projected density (upper left panel), line-of-sight velocity dispersion (lower left panel) and projected anisotropy parameter (lower right panel) profiles of the best-fitting Newtonian (red solid curves) and QUMOND (blue solid curves) models of NGC 5024. The dashed blue curve indicates the best-fitting QUMOND model assuming the minimum mass-to-light ratio  $(M/L_V)_{min} = 1.232$ . The black dots mark binned observational data for comparison, but the analysis has been conducted using unbinned data. The probability distributions of  $M/L_V$  for QUMOND models and of  $(M/L_V)_{min}$  are shown in the upper right panel with red and empty histograms, respectively. Mass-to-light ratios are in solar units.

a set of isochrones from the [Cassisi et al. \(2000\)](#) database with suitable metal content  $Z$  and age. These isochrones use a solar mixture and extend from very low mass stars ( $m \sim 0.1M_\odot$ ) to asymptotic giant branch stars and include mass loss occurring during cluster evolution. The metal content has been derived using the metallicities  $[Fe/H]$  from the [Harris \(1996, 2010\)](#) catalog, accounting for the effect of  $\alpha$ -enhancement

using the relation from [Salaris, Chieffi, & Straniero \(1993\)](#)

$$\log Z = \log(0.02) + [[Fe/H] + \log(0.638 f_\alpha + 0.362)]$$

with

$$f_\alpha = \begin{cases} 10^{0.28} & \text{if } [Fe/H] < -0.8 \\ 10^{-0.35 [Fe/H]} & \text{if } [Fe/H] > -0.8. \end{cases}$$

The age of each cluster has been derived by converting colors and magnitudes of isochrones of different ages into absolute magnitudes and dereddened colors using the distance of Baumgardt & Vasiliev (2021), the reddening of Harris (1996, 2010 edition) and the extinction coefficients by Cardelli, Clayton, & Mathis (1989). We choose the age providing the lowest  $\chi^2$ , calculated using the stars within 2 magnitudes from the turn-off point.

As stars of different masses contribute to the cluster mass and luminosity budget in a different way, it is essential to know their relative fraction (the present-day MF). We model the MF as a single power-law with slope  $\alpha_{MF}$ , which has been shown to be a good approximation for many GCs (Ebrahimi et al. 2020). In particular, we adopt the MF measured by Baumgardt et al. (2023).

We assume that mass dependent depletion of stars has turned an initial Kroupa (2001) MF into the observed MFs. We model the the passive evolution of the initial population, using the relations of Kruijssen (2009). According to these relations, stars above  $8 M_{\odot}$  evolve into neutron stars or into black holes depending on their original mass. However, most of these stars are expected to quickly escape from the system because of the natal kick occurring at the end of their evolution (Drukier 1996). As we want to estimate the minimum  $M/L_V$ , we exclude all stars with initial masses  $m > 8 M_{\odot}$ . The stars with  $m < 8 M_{\odot}$  become white dwarfs and do not suffer from natal kicks. The mass in main-sequence stars is computed by integrating the present-day MF between  $0.1 M_{\odot}$  and the turn-off mass. To this mass, we add the mass in white dwarfs, computed assuming that white dwarfs are lost at the same fraction as main-sequence stars of the same mass, and using the initial-final mass relation of Kalirai et al. (2008). The luminosities of all stars, derived from the best-fit isochrone, have been finally summed to provide  $L_V$ , and thus an estimate of  $M/L_V$  which is independent of the cluster dynamics.

Note that this  $M/L_V$  is a lower limit to the actual value, mainly because the mass in white dwarf is a lower limit. White dwarfs are being lost at a lower rate compared to main-sequence stars of the same mass, since they are more massive stars for a significant fraction of the time and, also when they turn into white dwarfs, they start from the centre, so it takes them a long time to drift towards the tidal radius.  $N$ -body simulations have shown that white dwarfs can contribute up to 70% of the total mass in an evolved cluster (see Fig. 11 of Baumgardt & Makino 2003). Instead, in our estimates of the present-day cluster mass, in which this effect is neglected, the contribution of white dwarfs never exceeds 25%.

For each cluster we repeat the above task  $10^3$  times by adding to cluster distances and metallicities a random shift extracted by Gaussian distributions centred on the nominal value and with a standard deviation equal to the  $1\sigma$  uncertainties quoted by Baumgardt & Vasiliev (2021) for distances and a typical value of 0.1 dex for metallicities. The distribution of the output  $(M/L_V)_{min}$  has been assumed as representative of the probability distribution of  $(M/L_V)_{min}$ .

For each GC  $10^6$  pairs (dynamical  $M/L_V$  and  $(M/L_V)_{min}$ ) have been extracted from the estimated distributions and the fraction of occurrences of dynamical  $M/L_V > (M/L_V)_{min}$  has been assumed as the probability  $P$  of compatibility between the data and the considered model.

## 5 RESULTS

The probability of agreement  $P$  for the 18 GCs of our sample is listed in Table 1 for both Newtonian and QUMOND models. None of the analysed clusters has been found with a dynamical  $M/L_V$  significantly incompatible ( $P < 0.003$ , corresponding to  $\sim 3\sigma$ ) with the predicted lower limit. For one of them (NGC5024) the QUMOND prediction lies at  $2.8\sigma$  below such a lower limit ( $P = 0.005$ ).

In Fig. 10 the dynamical  $M/L_V$  estimated by Newtonian and QUMOND models are compared with  $(M/L_V)_{min}$  and with the mass-to-light ratios measured by Baumgardt & Vasiliev (2021). The  $M/L_V$  of our Newtonian models are in good agreement with those of Baumgardt & Vasiliev (2021), with the exception of 3 GCs (NGC288, NGC4590 and NGC6779).

As expected, the Newtonian models are systematically more massive than QUMOND ones. As already discussed in Sect. 1, this is a direct consequence of the increased acceleration in MOND models, which therefore require less mass to keep the cluster in equilibrium. An exception is the cluster NGC6352, for which the Newtonian  $M/L$  is lower than the QUMOND  $M/L$ : this can be explained by the fact that for this cluster the QUMOND best fit has a lower anisotropy than the Newtonian one.

When comparing the dynamical  $M/L_V$  with the minimum ones estimated from stellar evolution, it is apparent that the  $M/L_V$  of Newtonian models are systematically higher than  $(M/L_V)_{min}$ , indicating a consistency between these models and independent observational constraints. The  $M/L_V$  of QUMOND models are on average closer to  $(M/L_V)_{min}$ . Remarkably, in QUMOND the cluster NGC5024 has a best-fitting dynamical  $M/L_V$  lower than  $(M/L_V)_{min}$ , thus showing a deficiency of mass (though contained within the uncertainties).

## 6 CONCLUSIONS

In this paper we developed dynamical models of stellar systems within the framework of the quasi-linear modified Newtonian dynamics (QUMOND), which include radial anisotropy in the same fashion as their analogues in the standard Newtonian dynamics (Gunn & Griffin 1979). We compared them with the most updated set of observational kinematics of a sample of 18 GCs located in the Galactic halo in a range of Galactocentric distances  $2.5 < R_{GC}/\text{kpc} < 18.5$ , a region characterized by external accelerations in the range  $0.32 < a_{ext}^N/a_0 < 4.88$  and derived their dynamical  $M/L_V$ . We then tested the validity of both Newtonian and QUMOND theories by comparing these values with independent lower limits derived through the use of synthetic stellar evolution models.

As reported in Sect. 5, none of the analysed clusters has a dynamical  $M/L_V$  formally incompatible ( $> 3\sigma$ ) with the minimum  $(M/L_V)_{min}$  prediction of stellar evolution models, although one of them (NGC5024) reaches a disagreement with the QUMOND prediction at  $2.8\sigma$ .

Considering that there is still room to improve the accuracy of the estimated  $M/L_V$  and their corresponding lower limits, it is possible that the incompatibility of this cluster (or others not sampled by our survey) could become significant when better data are available.

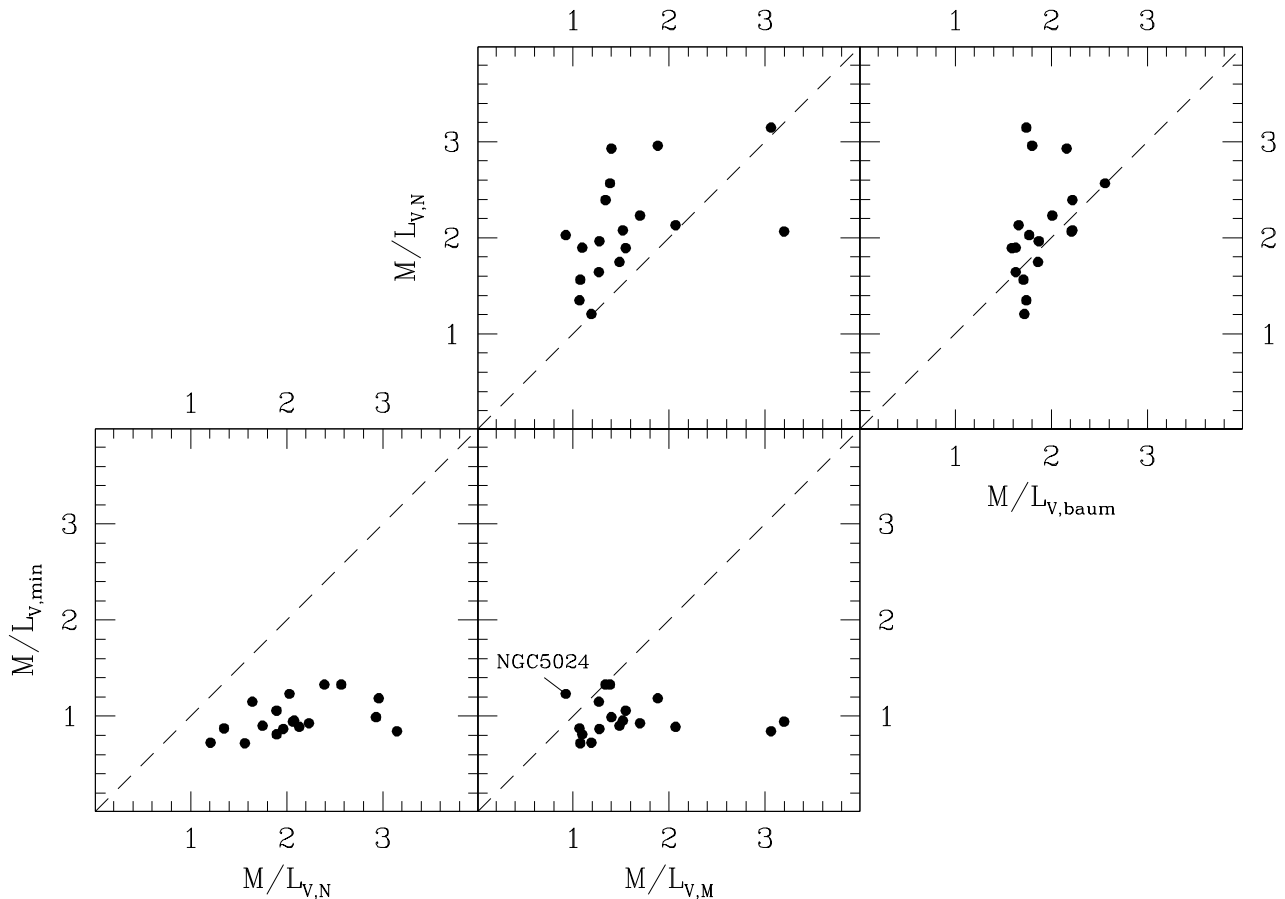


**Figure 10.** Comparison among different estimates of  $M/L_V$  (in solar units) for our sample of GCs. In the upper panels we compare the best-fitting Newtonian  $M/L_V$  with that of QUMOND (left panel) and that of Baumgardt & Vasiliev (2021) (right panel). In the lower panels we compare the minimum  $(M/L_V)_{min}$  with the best-fitting  $M/L_V$  of Newtonian (left panel) and QUMOND (right panel) models. The location of NGC5024 in the  $(M/L_V)_M$  vs.  $(M/L_V)_{min}$  plane is shown.

A limit of our QUMOND model is that we neglect the fact that the external field varies while a GC moves along its orbit. In particular, if the external field experienced by NGC5024 was stronger in the past, the kinematics of this object might retain memory of when it was in a more Newtonian regime, which in principle could help explain the low dynamical  $M/L_V$  found for our QUMOND model. However, this effect is expected to be unimportant because (i) the timescale over which the GC reacts to any change of the external field is typically much shorter than the orbital timescale (even for very eccentric orbits; Wu & Kroupa 2013) and (ii) NGC5024 should not experience strong variations of the external field because its orbit has a relatively low eccentricity of  $\approx 0.4$  (Vasiliev & Baumgardt 2021).

Binaries cannot solve the discrepancy found for NGC5024: the effect of such objects is to inflate the actual velocity dispersion because of the velocity oscillation of the primary component around the centre of mass that spuriously adds a spread to the actual velocity dispersion (see e.g. Bradford et al. 2011). So, the net effect would be to further decrease the required mass (and consequently the  $M/L_V$ ) needed to fit observations.

Similar considerations hold for the tidal heating. Also in this case, the kinetic energy released by the Galactic tidal field to the cluster stars would result in an increase of their velocity dispersion, thus enhancing the tension between predictions and observations (Spitzer & Chevalier 1973).

An opposite effect is instead produced by mass segregation. Indeed, the radial velocities available for most GCs are those of the red giant stars, which are the most massive stars of the sample. These stars tend to sink in the central region of the cluster because they tend to release kinetic energy to less massive stars. Therefore, they populate preferentially inner orbits with a velocity dispersion which, for a given mass, is lower than that predicted by single-mass models. So, by neglecting this effect, the best fit of the velocity dispersion neglects the contribution of the dynamically hot low-mass stars, resulting in an underestimated mass and  $M/L_V$  up to a factor of  $\sim 2$  (Sollima et al. 2017a). For this reason, even a formal disagreement could not falsify MOND theories until multi-mass models in this gravitational framework are developed. The models used in this paper can be generalized to allow for the presence of a spectrum of mass, as described in Gunn & Griffin (1979). However, multi-mass QUMOND



models of GCs would require some inputs from simulations with QUMOND collisional  $N$ -body codes, which, as far as we know, have not been developed so far (see Ciotti & Binney 2004 for a discussion of two-body relaxation in MOND).

Summarizing, although the present analysis is not able to provide firm conclusions on the validity of QUMOND, we show that this approach can be valuable for this purpose in the future. Indeed, while previous analyses (Ibata et al. 2011a; Sollima et al. 2012) were limited to only 2 GCs subject to a negligible external field, here we can include GCs populating the inner Galactic halo, enlarging the number of target clusters. Note that many GCs in this external acceleration range have promising properties (such as relatively steep MFs and low mass), but could not be included in our sample because of the lack of a significant number of radial velocities and/or proper motions with the required accuracy. The next releases of Gaia foresee an improvement in the accuracy and depth of proper motions (Gaia Collaboration et al. 2018a), and surveys of radial velocities are continuously in progress. This could further enlarge the number of available target GCs and decrease the width of the  $M/L_V$  probability distributions, thus improving the efficiency in detecting tensions between models and observations. On the theoretical side, the development of multi-mass QUMOND models will account for the effects of mass segregation, providing a more complete representation of real GCs.

## ACKNOWLEDGEMENTS

We warmly thank Michele Bellazzini for useful discussions and suggestions. We are grateful to an anonymous referee for constructive comments that helped improve the paper.

## DATA AVAILABILITY

The data underlying this article will be shared on reasonable request to the authors.

## REFERENCES

Anderson J., Sarajedini A., Bedin L. R., King I. R., Piotto G., Reid I. N., Siegel M., et al., 2008, *AJ*, 135, 2055  
 Angus G. W., Famaey B., Buote D. A., 2008, *MNRAS*, 387, 1470  
 Babcock H. W., 1939, *LicOB*, 498, 41  
 Baumgardt H., Makino J., 2003, *MNRAS*, 340, 227  
 Baumgardt H., Grebel E. K., Kroupa P., 2005, *MNRAS*, 359, L1  
 Baumgardt H., Hilker M., 2018, *MNRAS*, 478, 1520  
 Baumgardt H., Sollima A., Hilker M., 2020, *PASA*, 37, e046  
 Baumgardt H., Vasiliev E., 2021, *MNRAS*, 505, 5957  
 Baumgardt H., Hénault-Brunet V., Dickson N., Sollima A., 2023, *MNRAS*, 521, 3991  
 Bekenstein J. D., 2004, *PhRvD*, 70, 083509  
 Bekenstein J. D., 2009, *NuPhA*, 827, 555  
 Bekenstein J., Milgrom M., 1984, *ApJ*, 286, 7  
 Binney J., Tremaine S., 2008, in "Galactic Dynamics: Second Edition", Princeton University Press, Princeton, NJ  
 Bradford J. D., Geha M., Muñoz R. R., Santana F. A., Simon J. D., Côté P., Stetson P. B., et al., 2011, *ApJ*, 743, 167  
 Buote D. A., Canizares C. R., 1994, *ApJ*, 427, 86  
 Cardelli J. A., Clayton G. C., Mathis J. S., 1989, *ApJ*, 345, 245  
 Cassisi S., Castellani V., Ciarcelluni P., Piotto G., Zoccali M., 2000, *MNRAS*, 315, 679

Carmona-Benitez M. C., Akerib D. S., Araújo H. M., Bai X., Bailey A. J., Balajthy J., Beltrame P., et al., 2016, *NPPP*, 273-275, 309  
 Chae K.-H., Milgrom M., 2022, *ApJ*, 928, 24  
 Ciotti L., Binney J., 2004, *MNRAS*, 351, 285  
 Clowe D., Bradač M., Gonzalez A. H., Markevitch M., Randall S. W., Jones C., Zaritsky D., 2006, *ApJL*, 648, L109  
 Drukier G. A., 1996, *MNRAS*, 280, 498  
 Ebrahimi H., Sollima A., Haghi H., Baumgardt H., Hilker M., 2020, *MNRAS*, 494, 4226  
 Eilers A.-C., Hogg D. W., Rix H.-W., Ness M. K., 2019, *ApJ*, 871, 120  
 Faber S. M., Jackson R. E., 1976, *ApJ*, 204, 668  
 Faber S. M., Lin D. N. C., 1983, *ApJL*, 266, L17  
 Famaey B., Binney J., 2005, *MNRAS*, 363, 603  
 Famaey B., McGaugh S. S., 2012, *LRR*, 15, 10  
 Fraternali F., Sancisi R., Kamphuis P., 2011, *A&A*, 531, A64  
 Fridman A. M., Poliachenko V. L., 1984, in "Physics of gravitating systems. II - Nonlinear collective processes: Nonlinear waves, solitons, collisionless shocks, turbulence. Astrophysical applications", Springer-Verlag, New York  
 Gaia Collaboration, Brown A. G. A., Vallenari A., Prusti T., de Bruijne J. H. J., Babusiaux C., Bailer-Jones C. A. L., et al., 2018a, *A&A*, 616, A1  
 Gaia Collaboration, Helmi A., van Leeuwen F., McMillan P. J., Massari D., Antoja T., Robin A. C., et al., 2018b, *A&A*, 616, A12  
 Gaia Collaboration, Brown A. G. A., Vallenari A., Prusti T., de Bruijne J. H. J., Babusiaux C., Biermann M., et al., 2021, *A&A*, 649, A1  
 Gentile G., Famaey B., Angus G., Kroupa P., 2010, *A&A*, 509, A97  
 GRAVITY Collaboration, Abuter R., Amorim A., Anugu N., Bauböck M., Benisty M., Berger J. P., et al., 2018, *A&A*, 615, L15  
 Gunn J. E., Griffin R. F., 1979, *AJ*, 84, 752  
 Harris W. E., 1996, *AJ*, 112, 1487  
 Ibata R., Sollima A., Nipoti C., Bellazzini M., Chapman S. C., Dalessandro E., 2011a, *ApJ*, 738, 186  
 Ibata R., Sollima A., Nipoti C., Bellazzini M., Chapman S. C., Dalessandro E., 2011b, *ApJ*, 743, 43  
 Kalirai J. S., Hansen B. M. S., Kelson D. D., Reitzel D. B., Rich R. M., Richer H. B., 2008, *ApJ*, 676, 594  
 Karim T., Mamajek E. E., 2017, *MNRAS*, 465, 472.  
 Korsaga M., Epinat B., Amram P., Carignan C., Adamczyk P., Sorgho A., 2019, *MNRAS*, 490, 2977  
 Kent S. M., 1986, *AJ*, 91, 1301  
 King I. R., 1966, *AJ*, 71, 64  
 Kroupa P., 2001, *MNRAS*, 322, 231  
 Kruijssen J. M. D., 2009, *A&A*, 507, 1409  
 Jordi K., Grebel E. K., Hilker M., Baumgardt H., Frank M., Kroupa P., Haghi H., et al., 2009, *AJ*, 137, 4586  
 Lisanti M., Moschella M., Outmezguine N. J., Slone O., 2019, *PhRvD*, 100, 083009  
 Lüghausen F., Famaey B., Kroupa P., 2015, *CaJPh*, 93, 232  
 Mancera Piña P. E., Fraternali F., Oosterloo T., Adams E. A. K., Oman K. A., Leisman L., 2022, *MNRAS*, 512, 3230  
 Michie R. W., 1963, *MNRAS*, 125, 127  
 Milgrom M., 1983, *ApJ*, 270, 365  
 Milgrom M., 2010, *MNRAS*, 403, 886  
 Milgrom M., 2023, preprint (arXiv:2305.01589)  
 Miocchi P., Lanzoni B., Ferraro F. R., Dalessandro E., Vesperini E., Pasquato M., Beccari G., et al., 2013, *ApJ*, 774, 151  
 Mulchaey J. S., Davis D. S., Mushotzky R. F., Burstein D., 1993, *ApJL*, 404, L9  
 Mushotzky R. F., 1991, *AIPC*, 222, 394  
 Natarajan P., Zhao H., 2008, *MNRAS*, 389, 250  
 Nipoti C., Londrillo P., Ciotti L., 2007, *MNRAS*, 381, L104

- Nipoti C., Londrillo P., Zhao H., Ciotti L., 2007, MNRAS, 379, 597
- Nipoti C., Ciotti L., Binney J., Londrillo P., 2008, MNRAS, 386, 2194
- Nipoti C., Ciotti L., Londrillo P., 2011, MNRAS, 414, 3298
- Paust N. E. Q., Reid I. N., Piotto G., Aparicio A., Anderson J., Sarajedini A., Bedin L. R., et al., 2010, AJ, 139, 476
- Planck Collaboration, Aghanim N., Ashdown M., Aumont J., Baccigalupi C., Ballardini M., Banday A. J., et al., 2016, A&A, 596
- Planck Collaboration, Aghanim N., Akrami Y., Ashdown M., Aumont J., Baccigalupi C., Ballardini M., et al., 2020, A&A, 641, A6
- Powell M. J. D., 1964, The Computer Journal, 7, 155
- Prendergast K. H., Tomer E., 1970, AJ, 75, 674
- Prša A., Harmanec P., Torres G., Mamajek E., Asplund M., Capitaine N., Christensen-Dalsgaard J., et al., 2016, AJ, 152, 41
- Safarzadeh M., Loeb A., 2021, ApJL, 914, L37
- Salaris M., Chieffi A., Straniero O., 1993, ApJ, 414, 580
- Sanders R. H., McGaugh S. S., 2002, ARA&A, 40, 263
- Sanders R. H., 2012a, MNRAS, 419, L6
- Sanders R. H., 2012b, MNRAS, 422, L21
- Sarajedini A., Bedin L. R., Chaboyer B., Dotter A., Siegel M., Anderson J., Aparicio A., et al., 2007, AJ, 133, 1658
- Sirianni M., Jee M. J., Benítez N., Blakeslee J. P., Martel A. R., Meurer G., Clampin M., et al., 2005, PASP, 117, 1049
- Skordis C., Złošnik T., 2021, PhRvL, 127, 161302
- Smoot G. F., Bennett C. L., Kogut A., Wright E. L., Aymon J., Boggess N. W., Cheng E. S., et al., 1992, ApJL, 396, L1
- Sollima A., Nipoti C., 2010, MNRAS, 401, 131
- Sollima A., Nipoti C., Mastrobuono Battisti A., Montuori M., Capuzzo-Dolcetta R., 2012, ApJ, 744, 196
- Sollima A., Baumgardt H., Zocchi A., Balbinot E., Gieles M., Hénault-Brunet V., Varri A. L., 2015, MNRAS, 451, 2185
- Sollima A., Dalessandro E., Beccari G., Pallanca C., 2017a, MNRAS, 464, 3871
- Sollima A., Baumgardt H., 2017b, MNRAS, 471, 3668
- Sollima A., Baumgardt H., Hilker M., 2019, MNRAS, 485, 1460
- Spitzer L., Chevalier R. A., 1973, ApJ, 183, 565
- Stetson P. B., Pancino E., Zocchi A., Sanna N., Monelli M., 2019, MNRAS, 485, 3042
- The L. S., White S. D. M., 1988, AJ, 95, 1642
- Trager S. C., King I. R., Djorgovski S., 1995, AJ, 109, 218
- Tully R. B., Fisher J. R., 1977, A&A, 54, 661
- van de Ven G., van den Bosch R. C. E., Verolme E. K., de Zeeuw P. T., 2006, A&A, 445, 513
- van den Bergh S., Morbey C., Pazder J., 1991, ApJ, 375, 594
- Vasiliev E., Baumgardt H., 2021, MNRAS, 505, 5978
- Walker M. G., Mateo M., Olszewski E. W., Peñarrubia J., Evans N. W., Gilmore G., 2009, ApJ, 704, 1274
- Wilson C. P., 1975, AJ, 80, 175
- Wu X., Kroupa P., 2013, MNRAS, 435, 728
- Wu X.-P., Chiueh T., Fang L.-Z., Xue Y.-J., 1998, MNRAS, 301, 861
- XENON Collaboration, Aprile E., Aalbers J., Agostini F., Alfonsi M., Althueser L., Amaro F. D., et al., 2020, arXiv, arXiv:2011.10431
- Zwicky F., 1933, AChPh, 6, 110
- Zwicky F., 1937, ApJ, 86, 217

## APPENDIX A: COMPUTATION OF THE MODELS

In this appendix we describe in more details the computation of the models presented in Sect. 2.

Reminding the normalizations of parameters given in eq. 19, the QUMOND modified Poisson equation of eq. 12 can

be written as

$$\tilde{\nabla}^2 W_M = -9\nu\tilde{\rho} + \nu'\tilde{\nabla}y \cdot \left( \tilde{\nabla}W_N + \frac{\tilde{a}}{\xi} \right) \quad (\text{A1a})$$

$$= -9\tilde{\rho}_f, \quad (\text{A1b})$$

where  $\tilde{\nabla}^2 \equiv r_c^2 \nabla^2$ ,  $\tilde{\nabla} \equiv r_c \nabla$  and

$$\tilde{\rho}_f = \nu\tilde{\rho} - \frac{\nu'}{9}\tilde{\nabla}y \cdot \left( \tilde{\nabla}W_N + \frac{\tilde{a}}{\xi} \right). \quad (\text{A2})$$

As far as we use the simple interpolating function  $\mu(x) = x/(1+x)$ ,  $\nu(y)$  is given by eq. 10 and

$$\nu'(y) = -\frac{1}{y\sqrt{y^2+4y}}, \quad (\text{A3})$$

where

$$y = \|\xi\tilde{\nabla}W_N + \tilde{a}\| \quad (\text{A4})$$

in terms of dimensionless quantities.

We define the Newtonian and MOND potentials and densities as combinations Legendre polynomials (eq. 15)

$$W = \sum_{k=0}^N \tilde{u}_k(r) P_k(\theta),$$

$$\tilde{\rho} = \sum_{k=0}^N \tilde{g}_k(r) P_k(\theta),$$

where we normalized the functions  $u_k$  and  $g_k$  as

$$\tilde{u}_k = -\frac{u_k}{\sigma_K^2}$$

$$\tilde{g}_k = \frac{g_k}{\rho_0}$$

or, in expanded form,

$$\tilde{u}_0 = W_0 - 9 \left( \int_0^{\tilde{r}} \tilde{r} \tilde{g}_0 d\tilde{r} - \frac{1}{\tilde{r}} \int_0^{\tilde{r}} \tilde{r}^2 \tilde{g}_0 d\tilde{r} \right), \quad (\text{A5})$$

$$\tilde{u}_k = \frac{9}{2k+1} \left( \tilde{r}^k \int_{\tilde{r}}^{\infty} \tilde{r}^{1-k} \tilde{g}_k d\tilde{r} + \tilde{r}^{-1-k} \int_0^{\tilde{r}} \tilde{r}^{k+2} \tilde{g}_k d\tilde{r} \right), \quad (\text{A6})$$

and

$$\tilde{g}_k = \frac{2k+1}{2} \int_0^{\pi} \tilde{\rho} P_k \sin \theta d\theta. \quad (\text{A7})$$

Note that there are two sets of coefficients  $u_k$  and  $g_k$  for Newtonian and QUMOND, with the same functional definitions, but calculated using  $\rho$  of  $\rho_f$ , respectively. For simplicity, in the following we omit the suffixes N and M for  $u_k$  and  $g_k$ , keeping in mind that these coefficients are calculated for both Newtonian and MOND models.

At the first iteration, we choose  $W_{M,0}$ ,  $\xi$  and  $\tilde{a}$ , and assume  $N=0$ . This implies

$$\tilde{g}_0 = \tilde{\rho} \quad (\text{A8})$$

and then

$$\tilde{u}_0 = W_{N,0} - 9 \left( \int_0^{\tilde{r}} \tilde{r} \tilde{\rho} d\tilde{r} - \frac{1}{\tilde{r}} \int_0^{\tilde{r}} \tilde{r}^2 \tilde{\rho} d\tilde{r} \right). \quad (\text{A9})$$

The above model is spherical and can be easily integrated from the centre outward. Note that our input is  $W_{M,0}$  while the Newtonian potential at the centre is unknown. To overcome to this problem, we run a pre-iteration with  $W_{N,0} =$

$W_{M,0}$  and construct a model starting from the inner boundary conditions

$$\begin{aligned}\tilde{\rho} &= 1, \\ y &= |\tilde{a}|, \\ \frac{dW_N}{d\tilde{r}} &= 0.\end{aligned}\quad (\text{A10})$$

After substitution of variables and integration, eq.s 6, 7 and 8 can be written as functions of  $W$  and  $\tilde{r}_a$  as

$$\tilde{\rho} = \frac{\sqrt{\pi}e^W \operatorname{erf}(\sqrt{W}) + \sqrt{\pi}e^{-\tilde{r}_a^2 W} \frac{\operatorname{erfi}(\tilde{r}_a \sqrt{W})}{\tilde{r}_a^3} - 2\sqrt{W}(1+\tilde{r}_a^2)}{(1+\tilde{r}_a^2) [\sqrt{\pi} e^{W_0} \operatorname{erf}(\sqrt{W_0}) - \frac{2}{3}(2W_0+3)]}, \quad (\text{A11})$$

$$\sigma_r^2 = \sigma_K^2 \frac{j_0 - j_2}{(j_0 + j_2 \tilde{r}_a^2)} \quad (\text{A12})$$

and

$$\sigma_t^2 = \sigma_K^2 \frac{2j_0 + j_2 [(5 + 2W(1 + \tilde{r}_a^2))\tilde{r}_a^2 + 3] - 2W^{\frac{5}{2}}(1 + \tilde{r}_a^2)}{(j_0 + j_2 \tilde{r}_a^2)(1 + \tilde{r}_a^2)}, \quad (\text{A13})$$

where

$$\begin{aligned}j_0 &= \frac{3}{4} \sqrt{\pi} e^W \operatorname{erf}(\sqrt{W}) - \sqrt{W}(W + 3/2), \\ j_2 &= \frac{\frac{3}{4} \sqrt{\pi} e^{-\tilde{r}_a^2 W} \operatorname{erfi}(\tilde{r}_a \sqrt{W}) + \tilde{r}_a \sqrt{W} (\tilde{r}_a^2 W - 3/2)}{\tilde{r}_a^5},\end{aligned}$$

and  $\operatorname{erf}$  and  $\operatorname{erfi}$  are the real and imaginary error functions, respectively.

At each radial step, we calculate the quantities  $\rho$ ,  $\tilde{g}_0$ , and  $\tilde{u}_0$  using eq.s A11, A8, and A9, respectively. The value of  $W$  at the origin of the axes is adopted as  $W_{N,0}$ , and a new iteration is started using only the first two equations of A10, until the value of  $W_{N,0}$  converges within 1%.

Once the spherical zero-model is computed, it is used to compute  $u_k$  and  $g_k$  for the desired value of  $N$  through eq.s A6 and A7, respectively. For convenience, we report below the expansion in Legendre polynomials to compute the terms  $y$  and  $\tilde{\nabla}y \cdot (\tilde{\nabla}W_N + \frac{\tilde{a}}{\xi})$  needed in eq. A2:

$$y = \sqrt{\left( \xi \sum_{k=0}^N \frac{du_k}{d\tilde{r}} P_k + \tilde{a} \cos \theta \right)^2 + \left( \frac{\xi}{\tilde{r}} \sum_{k=0}^N \frac{dP_k}{d\theta} u_k + \tilde{a} \sin \theta \right)^2}$$

and

$$\begin{aligned}\tilde{\nabla}y \cdot \left( \xi \tilde{\nabla}W + \tilde{a} \right) &= \frac{1}{y} \left[ \left( \xi \sum_{k=0}^N \frac{du_k}{d\tilde{r}} P_k + \tilde{a} \cos \theta \right)^2 \sum_{k=0}^N \frac{d^2 u_k}{d\tilde{r}^2} P_k + \right. \\ &\frac{1}{\tilde{r}} \left( \frac{\xi}{\tilde{r}} \sum_{k=0}^N \frac{dP_k}{d\theta} u_k + \tilde{a} \sin \theta \right)^2 \left( \frac{1}{\tilde{r}} \sum_{k=0}^N \frac{d^2 P_k}{d\theta^2} u_k - \sum_{k=0}^N \frac{du_k}{d\tilde{r}} P_k \right) + \\ &\left. \frac{2}{\tilde{r}} \frac{du_k}{d\tilde{r}} \frac{dP_k}{d\theta} \left( \xi \sum_{k=0}^N \frac{du_k}{d\tilde{r}} P_k + \tilde{a} \cos \theta \right) \left( \frac{\xi}{\tilde{r}} \sum_{k=0}^N \frac{dP_k}{d\theta} u_k + \tilde{a} \sin \theta \right) \right].\end{aligned}$$

As already discussed in Sect. 2, because of the presence of the external field, the isodensity surfaces are asymmetric and elongated along the direction of the external field. So, at each iteration, the density profiles are shifted to match the origin

of axes with the centre of the system. The new density map is used as input to compute the updated values of  $u_k$  and  $g_k$ . The density profiles of different steps are then compared and a new iteration is started if the average variation exceeds 0.1% of the central density.

## APPENDIX B: COMPUTATION OF THE EXTERNAL FIELD

The properties of the external field for each GC depend on the adopted Galactic model. For simplicity, in this work we adopt a spherical Galactic model. This choice has some advantages. First, while in general

$$\nu(\|\nabla\phi_N/a_0\|)\nabla\phi_N = \nabla\phi_M + \nabla \times \mathbf{A}, \quad (\text{B1})$$

where  $\nabla \times \mathbf{A}$  is some unknown solenoidal field, in spherical symmetry the term  $\nabla \times \mathbf{A}$  vanishes and eq. 1 can be properly used. Second, in spherical symmetry the external field points everywhere towards the Galactic centre and its strength depends only on the Galactocentric distance. We assume that the QUMOND acceleration must reproduce the rotation velocity of the Galactic disk ( $v_{rot} = 229$  km/s; Eilers et al. 2019). So, from eq. B1, assuming  $\nabla \times \mathbf{A} = 0$ , we have

$$\nu(\|\nabla\phi_N^{MW}/a_0\|)\|\nabla\phi_N^{MW}\| = \frac{v_{rot}^2}{R_{GC}}, \quad (\text{B2})$$

where  $\phi_N^{MW}(R_{GC})$  is the Newtonian potential generated by a density distribution with QUMOND potential  $\phi_M^{MW}(R_{GC})$  such that  $\|\nabla\phi_M^{MW}\| = v_{rot}^2/R_{GC}$ . Eq. B2 can be solved numerically, providing for any given Galactocentric distance  $R_{GC}$  the associated value of  $\tilde{a} = a_{ext}^N/a_0 = \|\nabla\phi_N^{MW}\|/a_0$ .

This paper has been typeset from a  $\text{\TeX}/\text{\LaTeX}$  file prepared by the author.